Available online at www.sciencedirect.com
ScienceDirect
Physica D 233 (2007) 151–166
PHYSICA D
www.elsevier.com/locate/physd

Morphological stability analysis of the epitaxial growth of a circular island: Application to nanoscale shape control

Zhengzheng Hu, Shuwang Li, John S. Lowengrub*

Department of Mathematics, University of California at Irvine, Irvine, CA 92697, United States

Received 17 August 2006; received in revised form 11 May 2007; accepted 26 June 2007
Available online 30 June 2007

Communicated by H. Levine

Abstract

In this paper, we present a comprehensive morphological stability analysis of a single, epitaxially growing, perturbed circular island by using a Burton–Cabrera–Frank (BCF) island dynamics model. We show that there exists a critical deposition flux for which a single mode perturbation remains unchanged. In the absence of an additional far-field mass flux, there exists a naturally stabilizing radius, so that beyond this radius, growth is always stable. Up to this radius, taking fluxes larger than the critical flux results in instability. The presence of kinetics makes sufficiently small islands grow stably, even without line tension or surface diffusion. The presence of desorption further introduces a range of parameters and island radii for which both stable and unstable shrinkage may occur. The presence of a far-field mass flux in the BCF model can eliminate the naturally stabilizing radius and unstable growth may be achieved for a wide range of island radii. We then demonstrate how these results may be exploited to control the shape of the island using the deposition flux and far-field mass flux as control parameters.

Keywords: Epitaxial growth; Island dynamics; Morphological stability; Attachment–detachment; Desorption

1. Introduction

At the nanoscale, the surface of a crystalline solid is composed of atomic steps which separate terraces differing in height by a single lattice spacing. The steps provide the kink sites at which new atoms are incorporated into the crystal. During epitaxial growth, atoms are fluxed onto the surface of a crystal from a vapor using for example, molecular beam epitaxy. At the surface, some atoms are adsorbed (adatoms), diffuse across the terraces and finally reach the steps, while some other atoms desorb back into the gas phase, cf. Fig. 1. Epitaxial growth is a means to produce almost defect-free, high-quality single crystals that have a wide range of applications including advanced electronic and optoelectronic devices (e.g. see [2,3]). Growth however is subject to instabilities that can lead to irregular or wavy surface patterning (e.g. [13]). Therefore, an understanding of the morphological stability of step motion is crucial for the study of epitaxial growth.

Burton, Cabrera and Frank [1] first introduced a semi-discrete model (BCF), in which the growth direction is discrete but the lateral direction is continuous, to describe the diffusion of adatoms and the motion of steps during epitaxial growth of thin films. The BCF model, supplemented with later modifications and extensions, has been extensively investigated in trains of straight steps. For example, Bales and Zangwill [4] found that the asymmetry in the energy barriers of adatom attachment and detachment to and from steps may induce a morphological instability. Caflisch et al. [5] developed a model that captures the kinetics missing in the classical BCF model. Based on the kinetic model, Caflisch and Li [6] introduced a set of boundary conditions including line tension, attachment–detachment kinetic rates, and surface diffusion.

In 1969, Avignon and Chakraverty (AC) [7], following the Mullins and Sekerka [8] framework, performed a linear stability analysis of a circular nucleus surrounded by a supersaturated infinite matrix of diffusing adatoms in the absence of kinetics but in the presence of desorption. This problem is relevant to

* Corresponding author.
E-mail addresses: zhu@math.uci.edu (Z. Hu), lis@math.uci.edu (S. Li), lowengrb@math.uci.edu (J.S. Lowengrub).

0167-2789/$ - see front matter © 2007 Elsevier B.V. All rights reserved.
doi:10.1016/j.physd.2007.06.020

the early stages of epitaxial growth since small islands are often circular and widely separated [15,16]. By setting the density of the adatoms at infinity to be proportional to the deposition flux, they found that if the deposition flux is constant, then there are two critical radii R_l and R_l^* ($R_l^* > R_l$) depending on the deposition flux and wavenumber l, such that any perturbations are only unstable when the island radius is in between R_l and R_l^*. More recently, Li, Rätz and Voigt (LRV) [12] without considering desorption of adatoms, analyzed the linear stability of an isolated circular epitaxial island with kinetic boundary conditions, which is enclosed in a large, fixed circle with a flux-free boundary condition. LRV found that there exists a critical island size beyond which the growth is always stable. They also found that if either the line tension or the surface diffusion is present, small islands are always stable. Namely, the Bales–Zangwill instability does not occur.

In this paper, we extend the studies of AC [7] and LRV [12] to include a more complete set of physical effects. We consider the effects of kinetics, desorption and an additional far-field flux applied on the outer boundary of a large circle enclosing the island. This flux could arise due to the diffusion of adatoms from other regions of the thin film and as such, it is a simple model of the effect of far-field interactions on the island nanoenvironment. (See [9] for a more realistic boundary condition which is based on a self-consistent mean-field theory.) An analysis shows that the far-field flux boundary condition is equivalent to a time-dependent Dirichlet boundary condition. Our main results are summarized as follows.

We determine the critical flux for which the shape of the island when perturbed by a single mode remains unchanged during the evolution. This critical flux depends on the island radius and the mode wavenumber (as well as other parameters). An analysis of the critical flux reveals that for sufficiently small radii, growth is stable due to kinetics, even without line tension or surface diffusion, and that in the absence of a far-field flux, there exists a naturally stabilizing radius beyond which the growth is always stable in agreement with AC and LRV. Up to this naturally stabilizing radius, taking fluxes larger than the critical flux results in instability. In the presence of desorption, a new regime is introduced in which the island may shrink stably or unstably, with non-negative deposition fluxes. The presence of an additional uniform far-field flux, may eliminate the naturally stabilizing radius and result in unstable growth for a wide range of radii. We also determine the flux that makes a specific mode the fastest growing (or slowest decaying when the perturbation is decreasing) among all the modes. Inspired by the ideas in Cristini and Lowengrub [10] and Li et al. [11] who developed a theory to control the morphology of micro-scale crystals, we then present examples of how these results may be used to control the shape of the island using the deposition and far-field fluxes as control parameters.

This paper is organized as follows: in Section 2, we present the mathematical formulation. In Section 3, we study the linear stability of circular islands using a one-sided model for simplicity. In Section 4, we present parameter studies, including comparisons between the cases without/with desorption. We also examine the effect of the far-field flux. We extend the results to a two-sided model and present several examples by which our theory can be used to control the island shapes. Conclusions are given in Section 5.

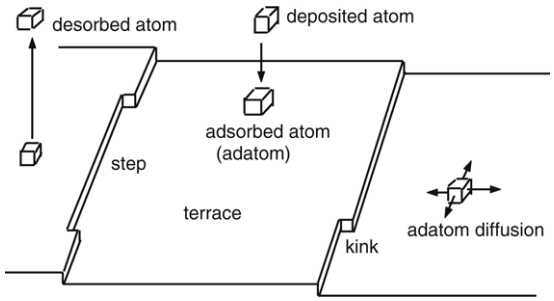

Fig. 1. Microscopic processes in the epitaxial growth of a thin film.

2. Mathematical formulation

2.1. The BCF model

Let $\rho_i = \rho_i(x, y, t)$ be the adatom concentration on a terrace $\Omega_i(t)$, where $i = 0, \ldots N$ is the discrete height of the layers. Then, the BCF model is

$$\partial_t \rho_i - \nabla \cdot (D \nabla \rho_i) = F - \tau^{-1} \rho_i \quad \text{in } \Omega_i(t), \tag{1}$$

where D is the diffusion constant, F is the deposition flux rate and τ^{-1} is the desorption rate. At the step edges $\Gamma_i(t)$, the adatom concentration satisfies the kinetic boundary conditions

$$-D \nabla \rho_i \cdot \mathbf{n}_i = k_+ \left(\rho_i - \rho^* (1 + \sigma \kappa_i)\right) \quad \text{on } \Gamma_i(t), \tag{2}$$

$$D \nabla \rho_{i-1} \cdot \mathbf{n}_i = k_- \left(\rho_{i-1} - \rho^* (1 + \sigma \kappa_i)\right) \quad \text{on } \Gamma_i(t), \tag{3}$$

where $\mathbf{n}_i$ is the unit normal pointing from the upper to lower terrace, k_+ and k_- are the kinetic attachment rates from the upper and lower terraces respectively, ρ^* is the equilibrium value of the adatom concentration for a straight step, σ is the line tension and κ_i is the curvature of $\Gamma_i(t)$.

We also assume that the upper and lower terraces are enclosed in a large, fixed circle Γ_∞ with radius R_∞, and an additional far-field flux J is imposed along the outer circle

$$\frac{1}{2\pi} \int_{\Gamma_\infty} D \nabla \rho_0 \cdot \mathbf{n} \mathrm{d}\Gamma = J \quad \text{on } \Gamma_\infty, \tag{4}$$

where $\mathbf{n}$ is the unit exterior normal at Γ_∞. The normal velocity of a step edge is given by

$$V_i = -D \nabla \rho_i \cdot \mathbf{n}_i + D \nabla \rho_{i-1} \cdot \mathbf{n}_i + \nabla_{s_i} \cdot (\nu \nabla_{s_i} \kappa_i) \quad \text{on } \Gamma_i(t), \tag{5}$$

where ν is the surface diffusion coefficient and $\nabla_{s_i} = (I - \mathbf{n}_i \mathbf{n}_i) \nabla$ is the surface gradient. See, [1,6,13,14] for details.

Here we will focus on the case in which the evolution is quasi-steady. That is, when the time scale for adatoms diffusion is much smaller than the time scale for deposition: $l_T^2 / D \ll 1/F$ where l_T is a typical terrace width. Under this assumption, Eq. (1) reduces to

$$-\nabla \cdot (D \nabla \rho_i) = F - \tau^{-1} \rho_i \quad \text{in } \Omega_i(t), \tag{6}$$

while the other equations do not change.

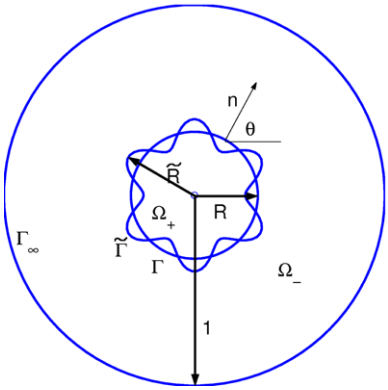

Fig. 2. The non-dimensional physical domain with a circular (radius R) and a perturbed (radius $\tilde{R}$) island.

2.2. Non-dimensionalization

Time and space are non-dimensionalized by using the diffusion time scale $t^* = R_\infty^2/D$ (assume D is constant) and the length scale $l^* = R_\infty$ which is the radius of Γ_∞. Defining the non-dimensional time and space variables as

$$\hat{t} = t/t^*, \qquad \hat{l} = l/l^*,$$

it follows that the non-dimensional BCF model is given by

$$-\hat{\Delta}\rho_i = \Lambda - \mu^2\rho_i, \quad \text{in } \hat{\Omega}_i(\hat{t}), \tag{7}$$

$$-\xi_+\hat{\nabla}\rho_i \cdot \mathbf{n}_i = \rho_i - \rho^*(1+\delta\hat{\kappa}_i) \quad \text{on } \hat{\Gamma}_i(\hat{t}), \tag{8}$$

$$\xi_-\hat{\nabla}\rho_{i-1} \cdot \mathbf{n}_i = \rho_{i-1} - \rho^*(1+\delta\hat{\kappa}_i) \quad \text{on } \hat{\Gamma}_i(\hat{t}), \tag{9}$$

$$\frac{1}{2\pi}\int_{\hat{\Gamma}_\infty} \hat{\nabla}\rho_0 \cdot \mathbf{n}\mathrm{d}\hat{\Gamma} = \Psi \quad \text{on } \hat{\Gamma}_\infty = 1, \tag{10}$$

$$\hat{V}_i = -\hat{\nabla}\rho_i \cdot \mathbf{n}_i + \hat{\nabla}\rho_{i-1} \cdot \mathbf{n}_i + \hat{\nabla}_{\hat{s}_i} \cdot (\beta\hat{\nabla}_{\hat{s}_i}\hat{\kappa}_i) \quad \text{on } \hat{\Gamma}_i(\hat{t}). \tag{11}$$

Note that ρ_i and ρ_{i-1} are already non-dimensional. The non-dimensional parameters in Eqs. (7)–(11) are

$$\Lambda = \frac{FR_\infty^2}{D}, \qquad \mu = \frac{R_\infty}{\sqrt{D\tau}}, \qquad \xi_\pm = \frac{D}{k_\pm R_\infty},$$
$$\delta = \frac{\sigma}{R_\infty}, \qquad \Psi = \frac{J}{D}, \qquad \beta = \frac{\nu}{DR_\infty},$$

which are non-dimensional measures of the deposition flux, the desorption rate, the attachment rates, the line tension, the far-field flux and the surface diffusion, respectively.

For simplicity, we will drop the hat notation to describe the non-dimensional model from now on.

3. Stability analysis

Following AC and LRV, we analyze the linear stability of a single circular island that is one lattice spacing in height (i.e., $N = 1$). Let us first consider a one-sided model, in which the adatom concentration is a constant on the upper terrace Ω_1. In Section 4.5, we give some results for the two-sided model. Our calculations suggest that the results are qualitatively similar for the one-sided and two-sided problems.

Consider a single circular island centered at the origin with non-dimensional radius $R(t)$ at time t (cf. Fig. 2). The upper terrace, i.e., the circular island, occupies $\Omega_+(t) = \Omega_1(t)$, and the lower terrace occupies $\Omega_-(t) = \Omega_0(t)$. The corresponding island boundary $\Gamma(t) = \Gamma_1(t)$ is the circle $r = R(t)$ with $r = |\mathbf{x}|/R_\infty$. The outer boundary Γ_∞ of the entire circular region $\overline{\Omega_+(t) \cup \Omega_-(t)}$ is the unit circle. We define $R_0 = R(0)$, with $0 < R_0 \ll 1$. The adatom concentration on the upper terrace and lower terrace are denoted by ρ_+ and ρ_-, respectively. Since the concentration is assumed to be constant on the upper terrace $\Omega_+(t)$, we only solve Eqs. (7) and (9)–(11).

Next consider a perturbation in both radial and angular directions (cf. Fig. 2),

$$\tilde{\rho}_-(r,\theta,t) = \rho_-(r,t) + \epsilon\rho_{-,1}(r,\theta,t), \tag{12}$$

$$\tilde{R}(\theta,t) = R(t) + \epsilon R_1(\theta,t), \tag{13}$$

where ϵ is a parameter small in magnitude. Denote by $\tilde{\Gamma}(t) = \{r = \tilde{R}(\theta,t)\}$, the perturbed island boundary and let $\tilde{\Omega}_-(t)$ be the perturbed lower terrace. The perturbations $R_1 = R_1(\theta,t)$ and $\rho_{-,1} = \rho_{-,1}(r,\theta,t)$ are periodic in the angular variable θ and can be written as

$$\rho_{-,1}(r,\theta,t) = \sum_{l=-\infty}^{+\infty} P_{-,1}(l,r,t)\mathrm{e}^{\mathrm{i}l\theta}, \tag{14}$$

$$R_1(\theta,t) = \sum_{l=-\infty}^{+\infty} R_{1,l}(t)\mathrm{e}^{\mathrm{i}l\theta}, \tag{15}$$

where for each integer wavenumber l, $R_{1,l}(t)$ and $P_{-,1}(l,r,t)$ are the Fourier coefficients. To study the linearized stability of the island, it suffices for us to consider the evolution of a single mode solution

$$\rho_{-,1}(r,\theta,t) = P_{-,1}(l,r,t)\mathrm{e}^{\mathrm{i}l\theta}, \tag{16}$$

$$R_1(\theta,t) = R_{1,l}(t)\mathrm{e}^{\mathrm{i}l\theta}, \tag{17}$$

for any positive integer wave number l.

To start, we plug Eqs. (12), (13), (16) and (17) into Eqs. (7) and (9)–(11) and get

- $O(1)$

$$\frac{1}{r}\partial_r(r\partial_r\rho_-) + \Lambda - \mu^2\rho_- = 0 \quad \text{in } \Omega_-(t), \tag{18}$$

$$\xi_-\partial_r\rho_- = \rho_- - \rho^*\left(1 + \frac{\delta}{R}\right) \quad \text{on } \Gamma(t), \tag{19}$$

$$\partial_r\rho_- = \Psi \quad \text{on } \Gamma_\infty, \tag{20}$$

$$V = \partial_r\rho_- \quad \text{on } \Gamma(t), \tag{21}$$

for the underlying radial solution and

- $O(\epsilon)$

$$\frac{1}{r}\partial_r(r\partial_r\rho_{-,1}) - \left(\frac{l^2}{r^2} + \mu^2\right)\rho_{-,1} = 0 \quad \text{in } \Omega_-(t), \tag{22}$$

$$\xi_-(R_1\partial_{rr}\rho_- + \partial_r\rho_{-,1}) = R_1\partial_r\rho_- + \rho_{-,1} + \frac{\rho^*\delta(1-l^2)R_1}{R^2} \quad \text{on } \Gamma(t), \tag{23}$$

$$\partial_r\rho_{-,1} = 0 \quad \text{on } \Gamma_\infty, \tag{24}$$

$$\partial_t R_1 = R_1\partial_{rr}\rho_- + \partial_r\rho_{-,1} - \frac{\beta(l^4-l^2)R_1}{R^4} \quad \text{on } \Gamma(t), \tag{25}$$

for the perturbation.

For simplicity, we assume the far-field flux $\Psi = 0$ in the following section, and we will discuss the effect of this flux in Section 4.3.

3.1. CASE1: No desorption ($\mu = 0$, $\Psi = 0$)

We first assume that the time for an adatom to reach a step is much smaller than the time scale to desorb, e.g. $\mu \ll 1$. This implies that the desorption term may be neglected. Under this assumption, Eqs. (18)–(21) give the following leading order (i.e., $O(1)$) solutions

$$\rho_-(r,t) = \frac{\Lambda}{4}(R^2 - r^2) + \frac{\Lambda}{2}\ln\left(\frac{r}{R}\right) + \rho^*\left(1 + \frac{\delta}{R}\right) + \frac{\Lambda\xi_-}{2R}(1 - R^2), \tag{26}$$

$$\dot{R}(t) = \frac{\Lambda}{2R}(1 - R^2), \tag{27}$$

where $\dot{R}(t) = \mathrm{d}R/\mathrm{d}t$. We first notice that $\dot{R}(t)$ is decreasing in R, which means a larger island grows more slowly than a smaller island. This is because the deposition is uniform, and as the island grows, there are more sites for the adatoms in the lower terrace to attach to, thus decreasing the adatom concentration gradient on the lower terrace. It follows from Eq. (27), the circular island achieves a steady-state, ie., $\dot{R}(t) = 0$, iff $\Lambda = 0$ or $R = 1$. Let us denote the steady-state flux by $\lambda^s(R) = 0$. Therefore, if $\Lambda > \lambda^s(R)$, the circular island will grow; and if $\Lambda < \lambda^s(R)$, the circular island will shrink.

Following Mullins and Sekerka [8], the growth rate of the lth mode perturbation relative to the evolving unperturbed circle is defined to be:

$$\mathrm{perrate}(l,t,R;\Lambda) = \left(\frac{R_{1,l}(t)}{R(t)}\right)^{-1}\frac{\mathrm{d}}{\mathrm{d}t}\left(\frac{R_{1,l}(t)}{R(t)}\right).$$

Then perturbations grow (decay) relative to the circle, with $\mathrm{perrate}(l,t,R;\Lambda) > 0$ ($\mathrm{perrate}(l,t,R;\Lambda) < 0$). Perturbations remain unchanged if $\mathrm{perrate}(l,t,R;\Lambda) = 0$. Physically, one parameter we may control is the non-dimensional deposition flux Λ (by varying the physical deposition flux F in time). Analogously, we may also potentially be able to control non-dimensional far-field flux Ψ (which is discussed in Section 4.3). Therefore, following Cristini and Lowengrub [10] and Li et al. [11], we determine the critical flux $\Lambda = \lambda(l,R)$, such that $\mathrm{perrate}(l,t,R;\lambda(l,R)) = 0$. Typically, this flux defines the boundary between stable and unstable evolution. Using the $O(1)$ solutions (Eqs. (26) and (27)), we solve the $O(\epsilon)$ equations (Eqs. (22)–(25)), and get the following equations for the perturbation growth rate $\mathrm{perrate}(l,t,R;\Lambda)$ and the critical flux $\lambda(l,R)$:

$$\mathrm{perrate}(l,t,R;\Lambda) = \frac{g(l,R)}{h(l,R)}(\Lambda - \lambda(l,R)), \tag{28}$$

where the critical flux $\lambda(l,R)$ is

$$\lambda(l,R) = \frac{q(l,R)}{g(l,R)}, \tag{29}$$

and

$$g(l,R) = l(R - \xi_-)(1 - R^2)(1 - R^{2l}) - 2R(1 + R^{2l}), \tag{30}$$

$$h(l,R) = 2R^2(\xi_- l(1 - R^{2l}) + R(1 + R^{2l})), \tag{31}$$

$$q(l,R) = \frac{\beta l^2(l^2 - 1)}{R^4}h(l,R) + 2\rho^*\delta l(l^2 - 1)(1 - R^{2l}). \tag{32}$$

In Section 4.1, the critical flux $\lambda(l,R)$ is plotted and analyzed further.

It is clear from Eqs. (28), (29) and (32) that the line tension and surface diffusion both tend to decrease the perturbation. This is because both effects tend to result in a motion of adatoms from the tip of a protrusion to a trough. Interface kinetics has a similar stabilizing effect. For example, if the tips are moving faster than the troughs, then the kinetics will help to increase the concentration around tips, thereby causing a net flux of adatoms from the tips to the troughs and also decreasing the concentration gradient in the lower terrace near the tips. We also notice that if deposition is absent, a perturbed island of any size is linearly stable. This is stated formally in the next theorem.

Theorem 1. *For any wavenumber $l \geq 1$, the steady-state circular island is always linearly stable.*

Proof. Let $l \geq 1$ and $\Lambda = \lambda^s(R) = 0$, then

$$\mathrm{perrate}(l,t,R;\lambda^s(R)) = -\frac{g(l,R)}{h(l,R)}\lambda(l,R) = -\frac{q(l,R)}{h(l,R)} \leq 0 \quad \text{for } 0 < R \leq 1. \quad \square$$

To understand the effect of the deposition flux requires an analysis of the sign of $g(l,R)$.

Proposition 1. *Let $\xi_- \geq 0$, if $l \leq 2$, or $l > 2$ and $\xi_- \geq 1$, then $g(l,R) < 0$ for $0 < R \leq 1$.*

Proof. (1) For $l = 1, 2$, since $0 < R \leq 1$, then $(1 - R^2)(1 - R^{2l}) < 1 + R^{2l}$. Also, since $\xi_- \geq 0$, we have $l(R - \xi_-) < 2R$, given $l = 1, 2$. Therefore $g(l,R) = l(R - \xi_-)(1 - R^2)(1 - R^{2l}) - 2R(1 + R^{2l}) < 0$, for $0 < R \leq 1$. (2) If $l > 2$ and $\xi_- \geq 1$, then it is clear from Eq. (30) that $g(l,R) < 0$ for $0 < R \leq 1$. $\square$

Proposition 1 tells us that if $l \leq 2$ or $\xi_- \geq 1$, the overall effect of the deposition flux decreases the perturbation. When the wavenumber $l \leq 2$, the island is an ellipse. In this case, it is preferable for adatoms to attach to the sides of the ellipse (arcs along the major axis) rather than at the tips. Therefore, islands always grow stably. Also, when $\xi_- \geq 1$, such that the effect of kinetics is strong, the islands grow stably for reasons described earlier.

For the case $0 \leq \xi_- < 1$ and $l > 2$, we solve $g(l,R) = 0$ for ξ_- and get $\xi_- = p(l,R)$ such that $g(l,R) = l(1 - R^2)(1 - R^{2l})(p(l,R) - \xi_-)$. In Fig. 3(a), $p(l,R)$ is plotted as a function of R for different wavenumbers l. Observe that

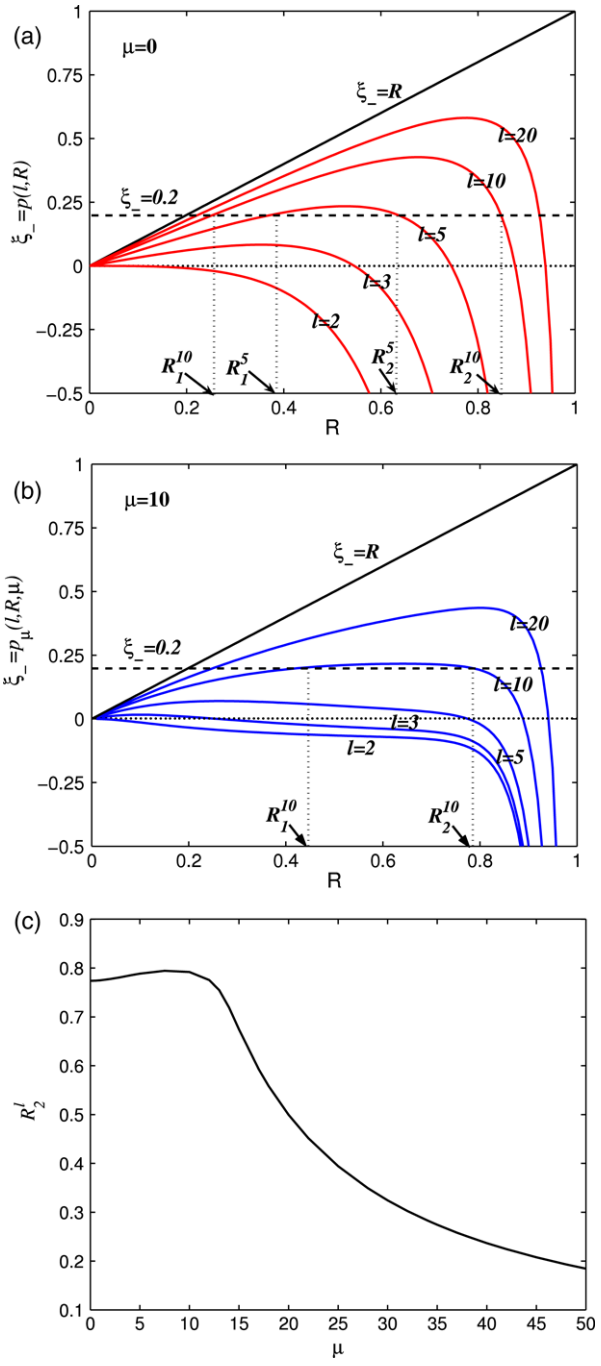

Fig. 3. (a) Graph of the function $p(l, R)$ for different wavenumbers l as indicated. (b) Graph of the function $p_\mu(l, R; \mu)$ for different wavenumbers l as indicated, and the desorption rates $\mu = 10$. (c) R_2^l such that $p_\mu(l, R_2^l; \mu) = 0.002$ with $l = 5$ is plotted as a function of μ in (μ, R)-plane.

$p(l, R)$ is an increasing function of l, while for each l, $p(l, R)$ is non-monotone in R. We also observe

Observation 1. Let $0 \le \xi_- < 1$,

(1) There exists $l^* = l^*(\xi_-) > 2$, such that, there exists a pair of radii R_1^l and R_2^l with $0 \le R_1^l < R_2^l$, so that $g(l, R_1^l) = g(l, R_2^l) = 0$ (i.e., $p(l, R_1^l) = p(l, R_2^l) = \xi_-$ for a given ξ_-) for any $l \ge l^*$. Take $\xi_- = 0.2$ as an example, then $l^* = 5$, $R_1^5 \approx 0.37388$ and $R_2^5 \approx 0.6354$. It is clear from Fig. 3(a) that, for any $l \ge 5$, there exists such a pair of radii R_1^l and R_2^l.

(2) We obtain $g(l, R) > 0$ for $R_1^l < R < R_2^l$, and $g(l, R) < 0$ for $0 < R < R_1^l$ (if $R_1^l > 0$) and $R > R_2^l$ with $l \ge l^*$; and $g(l, R) \le 0$ for $l < l^*$.

We therefore notice that regardless of whether the line tension or surface diffusion is present, a perturbed small island grows unstably between R_1^l and R_2^l provided that a large enough deposition flux is given ($\Lambda > \lambda(l, R)$). Outside this region of radii, island growth is always stable. The reason that a small island is always linearly stable is actually because of kinetics, which as mentioned before, slows down the growth of tips in general. In fact, small islands grow stably, even in the absence of surface diffusion or surface energy if there is a finite kinetic attachment rate. (See the remark below.) Moreover, as we mentioned before, the kinetics is proportional to the concentration gradients which are quite large when an island is very small, therefore the effect of the kinetics is much stronger when the island is smaller. This explains the existence of R_1^l, which is consistent with the results of LRV [12], and indicates that the Bales–Zangwill instability does not occur for small islands. On the other hand, a large island is also linearly stable because of the following two reasons. First, the deposition flux is uniform which maintains the adatom concentration outside the island. Secondly, as the island's size keeps increasing, the distance between tips increases, and since there are more attachment sites available to adatoms away from the tips, the tips grow more slowly than the inter-tip regions. This also implies that R_2^l is a naturally stabilizing radius (a proof is given in the next theorem), which is in agreement with AC [7] and LRV [12], who also concluded that large islands are always stable.

Theorem 2. *If $0 \le \xi_- < 1$ and $l \ge l^*(\xi_-)$, then there exists a radius R_2^l, beyond which* perrate$(l, t, R; \Lambda) \le 0$ *given $\Lambda \ge 0$. In other words, $R = R_2^l$ is a naturally stabilizing radius.*

Proof. Let $0 \le \xi_- < 1$ and $l \ge l^*(\xi_-)$, then the existence of R_2^l follows from Observation 1. Now by Eqs. (28), (29) and (32)

$$\text{perrate}(l, t, R_2^l; \Lambda) = -\frac{q(l, R_2^l)}{h(l, R_2^l)} = -\frac{\beta l^2(l^2-1)}{(R_2^l)^4} - \frac{2\rho^*\delta l(l^2-1)(1-(R_2^l)^{2l})}{h(l, R_2^l)} \le 0.$$

The last inequality holds because $h(l, R) > 0$ for any $0 < R \le 1$. Moreover, it follows from the Observation 1 that, if $R > R_2^l$, then $g(l, R) < 0$. Thus, by Eqs. (29), (30) and (32), $\lambda(l, R) < 0$. Therefore, perrate$(l, t, R; \Lambda) \le 0$ regardless of whether the deposition flux exists. □

We now summarize our conclusions as follows:

- A perturbed island always grows stably if one of the following conditions is satisfied: (1) the perturbation wavenumber $l \le 2$, (2) the kinetics coefficient $\xi_- \ge 1$, and (3) the kinetics coefficient $0 < \xi_- < 1$, and $l < l^*(\xi_-)$.
- If none of the above conditions is satisfied, a perturbed island grow unstably given a deposition flux larger than the critical

flux on (R_1^l, R_2^l), but outside that region of radii, the growth is always stable. As a special case, if $\xi_- = 0$, then $R_1^l = 0$. This means that small islands (initial radius $R_0 < R_2^l$) grow unstably given a sufficiently large deposition flux.

Remark. If the non-dimensional line tension $\delta = 0$ and the non-dimensional surface diffusion $\beta = 0$, then by Eqs. (32) and (29), $\lambda(l, R) = 0$. This implies that the sign of perrate$(l, t, R; \Lambda)$ is only decided by $g(l, R)$ for any positive non-dimensional flux Λ. It is clear from Fig. 3(a), if ξ_- is fixed, for each $R \in (\xi_-, 1)$, there exists a wavenumber $l^{**}(R)$ such that, $g(l, R) > 0$ for $l > l^{**}(R)$. In other words, in the absence of the line tension and the surface diffusion, islands perturbed with large wavenumber ($l > l^{**}$) always unstably grow if a positive deposition flux is imposed. We remark that this result qualitatively agrees with a proposition given in LRV [12].

Next we determine $\Lambda = \lambda^*(l, R)$ such that mode l is the fastest growing, if perrate$(l, t, R; \lambda^*(l, R)) > 0$ (and the slowest decaying, if perrate$(l, t, R; \lambda^*(l, R)) < 0$) among all the modes. It is expected that this mode will dominate the shape. A calculation shows that

$$\lambda^*(l, R) = \frac{a_1\rho^*\delta + a_2\beta}{a_3}, \tag{33}$$

where

$$\begin{aligned} a_1 &= 2R^2\left(2\xi_- l^3(1-R^{2l})^2 + (3l^2-1)R(1-R^{4l})\right. \\ &\quad \left. + 4l(l^2-1)R^{2l+1}\log\frac{1}{R}\right), \end{aligned} \tag{34}$$

$$a_2 = 4l(2l^2-1)(R(1+R^{2l}) + \xi_- l(1-R^{2l}))^2, \tag{35}$$

$$\begin{aligned} a_3 &= R^3(R(1-R^2) \\ &\quad + \xi_-(1+R^2))\left(1 - R^{4l} + 4lR^{2l}\log\frac{1}{R}\right). \end{aligned} \tag{36}$$

From the above expressions, it is clear that $\lambda^*(l, R) > 0$ for $0 < R \le 1$. We remark that $\lambda^*(l, R)$ only blows up at $R = 1$. Further, when perrate$(l, t, R; \lambda^*(l, R)) < 0$ such that perturbations decay, an analysis shows that $\lambda^*(l, R)$ is the flux that yields the slowest decay of mode l. In Section 4.1, both $\lambda(l, R)$ and $\lambda^*(l, R)$ are graphed and analyzed further.

3.2. CASE2: The effect of desorption ($\mu > 0$, $\Psi = 0$)

In this section, we consider the same single circular island as in CASE1 (cf. Fig. 2), and define a modified adatom concentration $\tilde{\omega}_- = \mu^2\tilde{\rho}_- - \Lambda$. The radius of the circle is now denoted as R_μ. For the sake of presentation, we define the following two auxiliary functions:

$$\begin{aligned} C_1(l, r) &= (I(l-1, \mu) + I(l+1, \mu))(K(l-1, \mu r) \\ &\quad + K(l+1, \mu r)) - (K(l-1, \mu) \\ &\quad + K(l+1, \mu))(I(l-1, \mu r) \\ &\quad + I(l+1, \mu r)), \\ C_2(l, r) &= (I(l-1, \mu) + I(l+1, \mu))K(l, \mu r) \\ &\quad + (K(l-1, \mu) + K(l+1, \mu))I(l, \mu r), \end{aligned}$$

where $I(l, x)$ is the modified Bessel function of the first kind, and $K(l, x)$ is the modified Bessel function of the second kind. The leading order solution $\omega_-(r, t; \mu) = \mu^2\rho_- - \Lambda$ and the velocity of the underlying circle $\dot{R}_\mu(t; \mu)$ are

$$\omega_-(r, t; \mu) = \frac{2\left(\mu^2\rho^*\left(1 + \frac{\delta}{R}\right) - \Lambda\right)}{\mu\xi_- C_1(0, R) + 2C_2(0, R)}C_2(0, r), \tag{37}$$

$$\dot{R}_\mu(t; \mu) = -\frac{(\mu^2\rho^*\left(1 + \frac{\delta}{R}\right) - \Lambda)}{2\mu(\mu\xi_- C_1(0, R) + 2C_2(0, R))}C_1(0, R). \tag{38}$$

Setting $\dot{R}_\mu(t; \mu) = 0$, we obtain the steady-state flux $\Lambda = \lambda_\mu^s(R; \mu) = \mu^2\rho^*(1 + \frac{\delta}{R})$. Note that $\lambda_\mu^s(R; \mu) > 0$ in contrast to the case without desorption. This is due to the fact that some adatoms desorb into the vacuum, thus a larger deposition flux is needed to grow the island.

Next, considering the $O(\epsilon)$ solutions lead to the expressions for the growth rate of the perturbation perrate$_\mu(l, t, R; \mu, \Lambda)$ and the critical flux $\lambda_\mu(l, R; \mu)$, we write them in a similar form as those in CASE1:

$$\text{perrate}_\mu(l, t, R; \mu, \Lambda) = \frac{g_\mu(l, R; \mu)}{h_\mu(l, R; \mu)}(\Lambda - \lambda_\mu(l, R; \mu)), \tag{39}$$

$$\lambda_\mu(l, R; \mu) = \frac{q_\mu(l, R; \mu)}{g_\mu(l, R; \mu)}, \tag{40}$$

where,

$$\begin{aligned} g_\mu(l, R; \mu) &= \frac{1}{4}(R - \xi_-)C_1(0, R)C_1(l, R) \\ &\quad - \left(RC_2(0, R) + \frac{C_1(0, R)}{\mu}\right)C_2(l, R), \end{aligned} \tag{41}$$

$$\begin{aligned} h_\mu(l, R; \mu) &= \frac{R}{4}(\mu\xi_- C_1(0, R) \\ &\quad + 2C_2(0, R))(\mu\xi_- C_1(l, R) + 2C_2(l, R)), \end{aligned} \tag{42}$$

$$\begin{aligned} q_\mu(l, R; \mu) &= \frac{\beta l^2(l^2-1)}{R^4}h_\mu(l, R; \mu) \\ &\quad + \mu^2\rho^*\left(1 + \frac{\delta}{R}\right)g_\mu(l, R; \mu) \\ &\quad + \frac{\mu\rho^*\delta(l^2-1)}{4R}(\mu\xi_- C_1(0, R) \\ &\quad + 2C_2(0, R))C_1(l, R). \end{aligned} \tag{43}$$

The flux $\lambda_\mu(l, R; \mu)$ is plotted in Section 4.1 (Fig. 5) and analyzed further there.

Similar to CASE1 ($\mu = 0$, $\Psi = 0$), when the steady-state flux is assumed, islands are always linearly stable. This is because, the desorption makes the net flux of adatoms to the island become zero and perturbations are stabilized by line tension and surface diffusion.

Theorem 3. *For any wavenumber $l \ge 1$, the steady-state circular island is always linearly stable.*

Proof. Let $l \ge 1$ and $\Lambda = \lambda_\mu^s(R; \mu)$, then

$$\text{perrate}_\mu(l, t, R; \mu, \lambda_\mu^s(R; \mu)) = -\frac{\beta l^2(l^2-1)}{R^4}$$

$$-\frac{\mu\rho^*\delta(l^2-1)(\mu\xi_- C_1(0,R)+2C_2(0,R))C_1(l,R)}{4h_\mu(l,R;\mu)R}$$
$$\le 0 \quad \text{for } 0<R\le 1.$$

The last inequality follows from the properties of Bessel functions. □

Following the strategy used in the previous section, we analyze the sign of $g_\mu(l,R;\mu)$. We write $g_\mu(l,R;\mu) = \frac{1}{4}C_1(0,R)C_1(l,R)\left(p_\mu(l,R;\mu)-\xi_-\right)$. In Fig. 3(b), the function $p_\mu(l,R;\mu)$ is plotted as a function of R for several values of l and $\mu = 10$. We also observe the following results that are qualitatively similar to CASE1.

Observation 2. Let $\xi_- \ge 0$ and $\mu > 0$,

(1) if $l \le 2$ or $\xi_- \ge 1$, then $g_\mu(l,R;\mu) \le 0$ for $0 < R \le 1$.

(2) if $l > 2$ and $0 \le \xi_- < 1$, then there exists a wavenumber $l^*_\mu = l^*_\mu(\xi_-,\mu) > 2$, such that, there exists a pair of radii R^l_1 and R^l_2, so that $g(l,R^l_1;\mu) = g(l,R^l_2;\mu) = 0$ for any $l \ge l^*_\mu$. For example, take $\xi_- = 0.2$ and $\mu = 10$, then $l^*_\mu = 10$, $R^{10}_1 \approx 0.431$, and $R^{10}_2 \approx 0.788$ (cf. Fig. 3(b)). We remark that $l^*_\mu > l^*$ for the same set of parameters (l^* is defined in Observation 1). Therefore $g(l,R;\mu) > 0$ for $R^l_1 < R < R^l_2$, and $g(l,R;\mu) < 0$ for $0 < R < R^l_1$ (given $R^l_1 > 0$) and $R > R^l_2$ with $l \ge l^*_\mu$; $g(l,R;\mu) \le 0$ for $l < l^*_\mu$.

We can also show that R^l_2 is a naturally stabilizing radius during growth.

Theorem 4. *If $0 \le \xi_- < 1$ and $l \ge l^*_\mu(\xi_-,\mu)$, then there exists a radius R^l_2, beyond which* $\text{perrate}_\mu(l,t,R;\mu,\Lambda) \le 0$ *given $\Lambda \ge \lambda_\mu(l,R;\mu)$.*

Proof. The existence of R^l_2 has been shown in Observation 2. By Eqs. (39)–(43), we have

$$\text{perrate}_\mu(l,t,R^l_2;\mu,\Lambda) = -\frac{q_\mu(l,R^l_2;\mu)}{h_\mu(l,R^l_2;\mu)} = -\frac{\beta l^2(l^2-1)}{(R^l_2)^4}$$
$$-\frac{\mu\rho^*\delta(l^2-1)(\mu\xi_- C_1(0,R^l_2)+2C_2(0,R^l_2))C_1(l,R^l_2)}{4h_\mu(l,R^l_2;\mu)R^l_2}$$
$$\le 0.$$

The last inequality holds because $h_\mu(l,R;\mu) > 0$ for any $0 < R \le 1$. Moreover, it follows from Observation 2(2) that, if $R > R^l_2$, then $g(l,R;\mu) \le 0$ for $l \ge l^*_\mu(\xi_-,\mu)$. Thus, by Eq. (39), if a flux $\Lambda \ge \lambda_\mu(l,R;\mu)$ is given, then $\text{perrate}_\mu(l,t,R;\mu,\Lambda) \le 0$. Therefore, R^l_2 is a naturally stabilizing radius. □

According to Eqs. (40) and (43) and properties of Bessel Functions, we next notice that

Observation 3. (1) $\lambda_\mu(l,R;\mu) \ge \lambda^s_\mu(R;\mu) > 0$, if $g_\mu(l,R;\mu) > 0$, and

(2) $\lambda_\mu(l,R;\mu) \le \lambda^s_\mu(R;\mu)$, if $g_\mu(l,R;\mu) < 0$.

This means that an island will grow unstably if and only if $g_\mu(l,R;\mu) > 0$ and $\Lambda > \lambda_\mu$. This behavior is qualitatively similar to CASE1. If we compare Fig. 3(a) with Fig. 3(b), it is clear that the unstable growth region is much narrower when the desorption is present. For example, let $l = 10$, then $R^{10}_1 \approx 0.27409$ and $R^{10}_2 \approx 0.84755$ if $\mu = 0$, whereas, $R^{10}_1 \approx 0.431$, and $R^{10}_2 \approx 0.788$ if $\mu = 10$. In Fig. 3(c), the naturally stabilizing radius R^l_2 is plotted as a function of μ for $l = 5$ and $\xi_- = 0.002$. We notice that R^l_2 depends non-monotonically on μ, though R^l_1 is an increasing function of μ for a fixed wavenumber l. This is because desorption tends to stabilize the growth by decreasing the effective deposition flux to the island in general. If the desorption is not sufficiently large, it may just be able to shift the unstable growth region toward a range of larger radii. However, once the desorption is sufficiently large, it will dramatically shrink the possibly unstable growth region for a fixed set of parameters.

In addition, a new regime is introduced by desorption: an unstable shrinkage may occur when $g_\mu(l,R;\mu) < 0$, because $\lambda^s_\mu(R;\mu) > 0$. According to our analysis (see Appendix A), for $R > R^l_2$, in contrast to CASE1, there exists another critical radius $R = R^l_c$ depending on all other parameters, such that $\lambda_\mu(l,R;\mu) > 0$ for $R \in (R^l_c,1)$, given $\mu^2 > \frac{\beta l^2(l^2-1)}{\rho^*(1+\delta)}$. During shrinkage, when this condition is satisfied, more adatoms will desorb back into the vacuum around the troughs, provided the distance between the tips is sufficiently large, resulting in instability. This also explains the existence of R^l_c. We therefore conclude that

Theorem 5. *Let $\beta \ge 0$, $l > 1$, and $\mu^2 > \frac{\beta l^2(l^2-1)}{\rho^*(1+\delta)}$, then there exists a critical radius $R^l_c > R^l_2$, such that if the deposition flux $\Lambda \in [0,\lambda_\mu(l,R;\mu))$, then $\dot{R}_\mu(t;\mu) < 0$, and* $\text{perrate}_\mu(l,R;\mu,\Lambda) > 0$ *on $(R^l_c,1)$. That is there exists unstable shrinkage on $(R^l_c,1)$.*

Proof. By Eq. (38), we get

$$\dot{R}_\mu(t;\mu) = -\frac{\left(\mu^2\rho^*\left(1+\frac{\delta}{R}\right)-\Lambda\right)}{2\mu(\mu\xi_- C_1(0,R)+2C_2(0,R))}C_1(0,R)$$
$$< -\frac{\left(\mu^2\rho^*\left(1+\frac{\delta}{R}\right)-\lambda(l,R;\mu)\right)}{2\mu(\mu\xi_- C_1(0,R)+2C_2(0,R))}C_1(0,R)$$
$$= \tilde{C}C_1(0,R),$$

where $\tilde{C} = \frac{\beta l^2(l^2-1)h_\mu(l,R;\mu)}{2\mu R^4(\mu\xi_- C_1(0,R)+2C_2(0,R))g_\mu(l,R;\mu)} + \frac{2\rho^*\delta(l^2-1)C_1(l,R)}{Rg_\mu(l,R;\mu)}$. Since $g_\mu(l,R;\mu) < 0$ for $R \in (R^l_c,1)$, we conclude that $\dot{R}_\mu(t;\mu) < 0$ for $R \in (R^l_c,1)$. This shows an island with radius $R_0 \in (R^l_c,1)$ shrinks. Moreover, by the comments before this theorem, we know that $\lambda_\mu(l,R;\mu) > 0$, if $\mu^2 > \frac{\beta l^2(l^2-1)}{\rho^*(1+\delta)}$. Thus, it follows from Eq. (39) that $\text{perrate}_\mu(l,R;\mu,\Lambda) > 0$ when $R \in (R^l_c,1)$ given a deposition flux $\Lambda \in [0,\lambda_\mu(l,R;\mu))$. □

We now summarize our conclusions as follows:

- The conclusions drawn in CASE1 are still true if the desorption is not sufficiently large, i.e., $\mu^2 < \frac{\beta l^2(l^2-1)}{\rho^*(1+\delta)}$.
- In contrast to CASE1, there exists a region of radii on which a perturbed island shrinks unstably if the conditions given in Theorem 5 are satisfied.

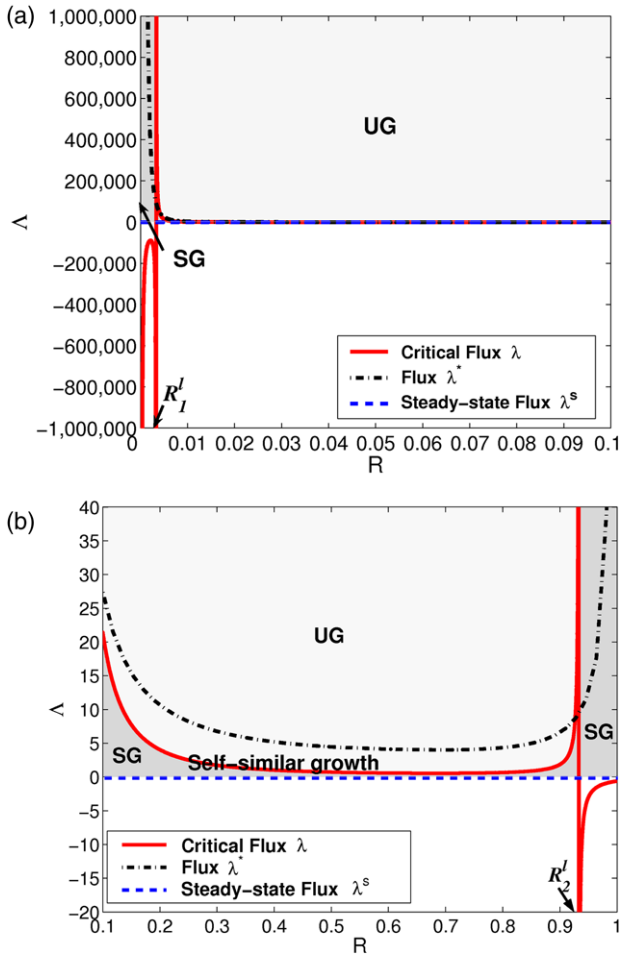

Fig. 4. The stability diagram and the flux $\lambda^*(l, R)$ in the (Λ, R)-plane for CASE1 ($\mu = 0$, $\Psi = 0$). (a) shows the region $0 < R < 0.1$, (b) shows the region $0.1 < R < 1$. The curve $\Lambda = \lambda(l, R)$ (solid), separates the stable growth region (shaded and marked by 'SG') and the unstable growth region (shaded and marked by 'UG'). R_2^l is the naturally stable radius. The dash-dotted line plots the flux $\lambda^*(l, R)$ such that mode l is the fastest growing, if $\text{perrate}(l, R; \lambda^*(l, R)) > 0$ (and the slowest decaying, if $\text{perrate}(l, R; \lambda^*(l, R)) < 0$) among all modes. The dashed line plots the steady-state flux $\lambda^s(R) = 0$. The parameters are: $\xi_- = 0.002$, $\rho^* = 1$, $\delta = 0.01$, $\beta = 10^{-4}$, $l = 5$.

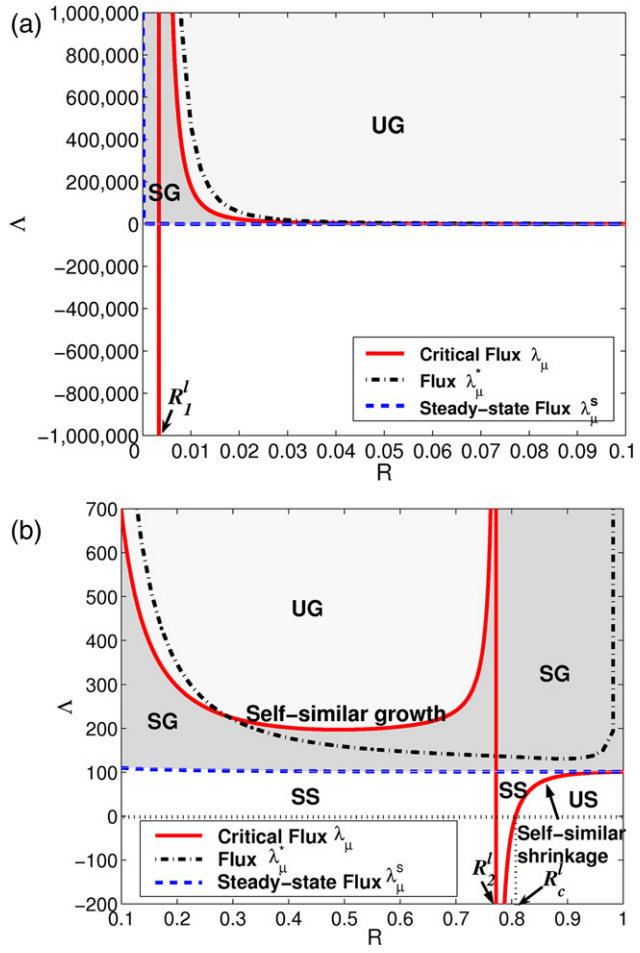

Fig. 5. The stability diagram and the flux $\lambda^*_\mu(l, R; \mu)$ in the (Λ, R)-plane for the CASE2 ($\mu > 0$, $\Psi = 0$). The curve $\Lambda = \lambda_\mu(l, R; \mu)$ (solid), separates the stable growth region (shaded and marked by 'SG') and the unstable growth region (shaded and marked by 'UG'). In contrast to the CASE1, it also separates the stable growth or shrinkage region (marked by 'SS') and the unstable shrinkage region (marked by 'US'). R_2^l is the naturally stabilizing radius. The dash-dotted line plots the flux $\lambda^*_\mu(l, R; \mu)$ such that mode l is the fastest growing, if $\text{perrate}_\mu(l, R; \mu, \lambda^*_\mu(l, R; \mu)) > 0$ (and the slowest decaying, if $\text{perrate}_\mu(l, R; \mu, \lambda^*_\mu(l, R; \mu)) < 0$) among all modes. The dashed line plots the steady-state flux $\lambda^s_\mu(R; \mu)$, which separates the growth region from the shrinkage region. The parameters are: $\mu = 10$, $\xi_- = 0.002$, $\rho^* = 1$, $\delta = 0.01$, $\beta = 10^{-4}$, $l = 5$.

As in CASE1, we can determine the flux $\Lambda = \lambda^*_\mu(l, R; \mu)$ such that mode l is the fastest growing, if $\text{perrate}_\mu(l, R; \mu, \lambda^*_\mu(l, R; \mu)) > 0$ (and the slowest decaying, if $\text{perrate}_\mu(l, R; \mu, \lambda^*_\mu(l, R; \mu)) < 0$) among all modes. The explicit form of $\lambda^*_\mu(l, R; \mu)$ is quite complicated and is not shown here. In the next section, $\lambda^*_\mu(l, R; \mu)$ is plotted and analyzed further.

4. Parameter investigation

4.1. Comparison between CASE1 and CASE2

An analysis of the results shows that $\lim_{\mu\to 0} \lambda_\mu(l, R; \mu) = \lambda(l, R)$, and likewise for the perturbation growth rate (perrate_μ). However, from Theorem 5, when $R \in (R_c^l, 1)$, $\lambda_\mu(l, R; \mu) > 0$. Consequently, if $0 \le \Lambda < \lambda_\mu(l, R; \mu)$, then $\text{perrate}_\mu(l, R; \mu, \Lambda) > 0$, and $\dot{R}_\mu(t; \mu) < 0$. However, in CASE1, $\lambda(l, R) \le 0$, $\text{perrate}(l, R) \le 0$, and $\dot{R}(t) \ge 0$, when $R > R_2^l$ ($< R_c^l$). Thus, in the absence of desorption, whenever $\Lambda > 0$, the circular island grows and is linearly stable (see Fig. 4). In contrast, when the desorption is present, one may have unstable shrinkage (see Fig. 5).

In Fig. 4, a typical stability diagram is plotted, showing the critical flux $\lambda(l, R)$ (solid) versus the radius R in the case without desorption (CASE1, $\mu = 0$, $\Psi = 0$), where $\xi_- = 0.002$, $\rho^* = 1$, $\delta = 0.01$, $\beta = 10^{-4}$, $l = 5$. (a) shows $R \in (0, 0.1)$, (b) shows $R \in (0.1, 1)$. A constant deposition flux Λ corresponds to a horizontal line in the diagram. In the shaded regions marked by UG and SG, there is unstable and stable growth, respectively. Note that (a) shows that the leftmost transition between SG and UG occurs at $R = R_1^l$, and the rightmost transition between UG and SG occurs at $R = R_2^l$ (shown in (b)). Our analysis also shows that R_1^l

and R_2^l are decreasing and increasing in l, respectively. This means that an island perturbed with a larger wavenumber l has a wider unstable growth region. The dash-dotted line on this graph marks the flux $\lambda^*(l, R)$ such that mode l is the fastest growing, if perrate$(l, t, R; \Lambda) > 0$ (and the slowest decaying, if perrate$(l, t, R; \Lambda) < 0$) among all modes. We remark that this flux blows up at boundary ($R = 1$).

In Fig. 5, the corresponding diagram is shown for CASE2 ($\mu \neq 0$, $\Psi = 0$). The non-dimensional desorption rate $\mu = 10$, while the other parameters are same as in Fig. 4. Note that $\mu^2 > \frac{\beta l^2(l^2-1)}{\rho^*(1+\delta)} = 0.06$, so that there exists an R_c^l such that $\lambda_\mu(l, R; \mu) > 0$ on $(R_c^l, 1)$. Compared to CASE1, 2 new regions with $\Lambda > 0$ arise: *stable shrinkage (marked by SS) and unstable shrinkage (marked by US)*. The dash-dotted line represents the flux $\lambda_\mu^*(l, R; \mu)$. Compared with the flux $\lambda^*(l, R)$ in Fig. 4, we observe that $\lambda^*(l, R) < \lambda_\mu^*(l, R; \mu)$ which indicates that a larger flux is needed to keep lth mode as the fastest growing (or slowest decaying) mode when desorption is present (note the large scale on the axes). Notice that this flux also blows up at boundary ($R = 1$). Also note that $\lambda_\mu < 0$ is not seen in (a) for $R \in (0, R_1^l)$, this is because it is still off the scale.

In Fig. 6(a), the velocities $\dot{R}(t)$ under the flux $\lambda^*(l, R)$ (solid) and $\dot{R}_\mu(t; \mu)$ under the flux $\lambda_\mu^*(l, R; \mu)$ (dashed) are plotted. It is clear that the island always grows. We remark that both velocities are not defined at boundary. We also remark that for the sake of better presentation, we have truncated the range of radii $R \in (0, 0.1)$, on which the scale is too large to show. In Fig. 6(b), the perturbation rates perrate$(t, l, R; \lambda^*(l, R))$ (solid) and perrate$_\mu(t, l, R; \mu, \lambda_\mu^*(l, R; \mu))$ (dashed) are plotted. Observe that the perturbation becomes stable (perrate$_\mu < 0$) at smaller radii when desorption is present. We remark that the region of radii which is not shown ($R \in (0, 0.1)$), includes $(0, R_1^l)$, on which both perrate and perrate$_\mu$ are negative. Since the discussions given in the next subsection are also based on the same set of parameters, we will omit the behaviors in this region for the sake of presentation. Next we analyze the dependence of the results on ξ_-, l and μ.

4.2. Dependence on ξ_-, l and μ

Dependence on ξ_-. It is clear from Fig. 3 that, $R_1^l = 0$ if non-dimensional kinetics from the lower terrace vanishes (i.e., $\xi_- = 0$). Therefore, the appearance of kinetics, which gives a limiting rate for adatom attachment to the island, narrows the unstable growth region and stabilizes the growth of small islands. We remark that the kinetics stabilizes small islands even without the line tension or surface diffusion. On the other hand, during the shrinkage, the kinetics acts to destabilize perturbations. This is because narrowing of the unstable growth region may widen the unstable shrinkage region. This can also be seen through the dependence of the critical flux upon the kinetics. According to Eqs. (30), (32), (41) and (43), the kinetics increases the critical flux $\lambda(l, R)$ and $\lambda_\mu(l, R; \mu)$, such that a larger deposition flux is required to make the perturbations grow compared with the case in which the kinetics is not present. Therefore, the overall effect

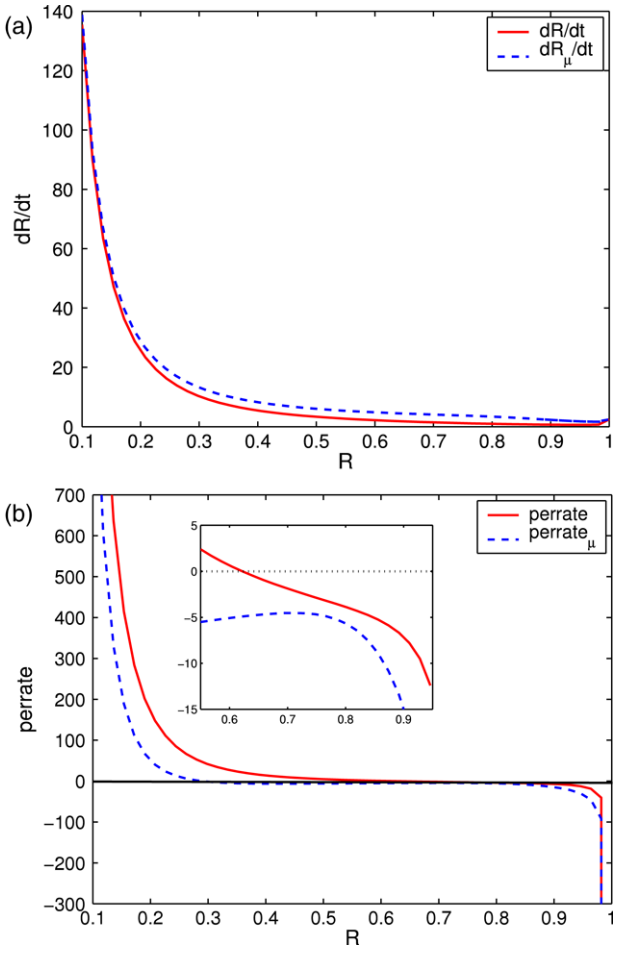

Fig. 6. (a) The velocity of the underlying circle under the fluxes $\lambda^*(l, R)$ (solid) and $\lambda_\mu^*(l, R; \mu)$ (dashed). (b) The growth rates using the fluxes $\lambda^*(l, R)$ (solid) and $\lambda_\mu^*(l, R; \mu)$ (dashed). The parameters are: $\mu = 10$, $\xi_- = 0.002$, $\rho^* = 1$, $\delta = 0.01$, $\beta = 10^{-4}$, $l = 5$.

of the kinetics is to decrease the perturbations during growth and increase the perturbations during shrinkage.

Dependence on l. In Fig. 7, the critical flux $\lambda_\mu(l, R; \mu)$ is plotted for several values of wavenumber l (the other parameters are the same as in Fig. 5). Observe that if the flux Λ is constant, then for each l, there exists two critical radii R_l and R_l^* such that the lth mode perturbation is unstable for $R_l < R < R_l^*$, and stable for $R \in (0, R_l] \cup [R_l^*, 1]$. This agrees with AC [7]. For the constant flux $\Lambda = 400$, R_4 and R_4^* are indicated in the plot. As in the Mullins–Sekerka theory of crystal growth, R_l is an increasing function of l. The second critical radius R_l^* does not exist in the classical Mullins–Sekerka theory and also is an increasing function of l. Together, these results imply that when R is small, there exists a critical wavenumber $l_c(R)$ such that for $l < l_c(R)$, the lth mode perturbation is unstable (and otherwise is stable). On the other hand, when R is large, there exists another critical wavenumber $l_c^*(R)$ such that if $l_c^*(R) < l < l_c(R)$, then the lth mode is unstable. We also observe that R_l and R_l^* are increasing and decreasing in ξ_-, respectively. This again proves that kinetics stabilizes perturbations during the growth.

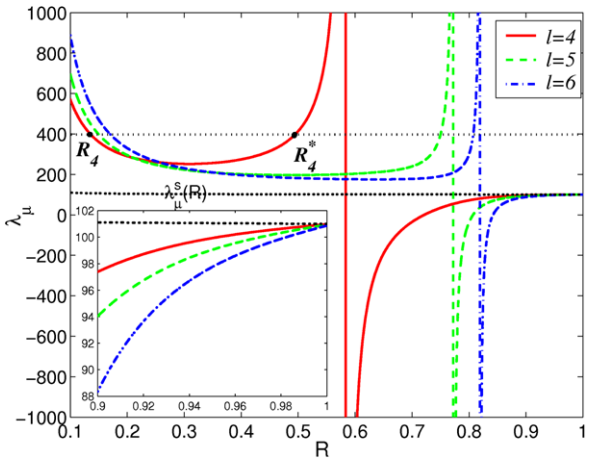

Fig. 7. The critical fluxes $\lambda_\mu(l, R; \mu)$ are plotted as functions of radius R for different wavenumbers: $l = 4, 5, 6$. The parameters are: $\mu = 10$, $\xi_- = 0.002$, $\rho^* = 1$, $\delta = 0.01$, $\beta = 10^{-4}$.

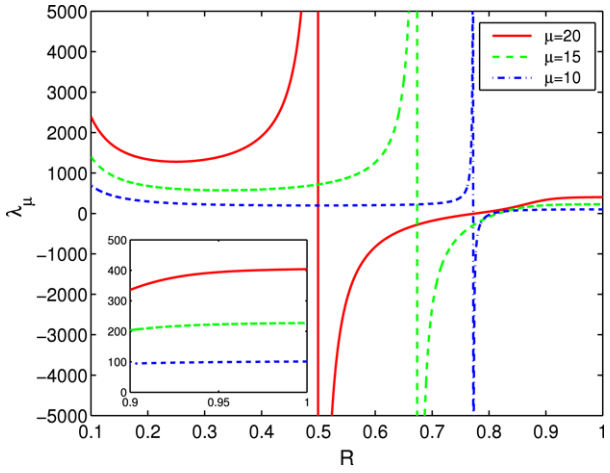

Fig. 8. The critical fluxes $\lambda_\mu(l, R; \mu)$ with an inset showing the behavior near $R \approx 1$ with $\mu = 10, 15, 20$. The parameters are: $\xi_- = 0.002$, $\rho^* = 1$, $\delta = 0.01$, $\beta = 10^{-4}$.

Dependence on μ. In Fig. 8, the critical flux $\lambda_\mu(l, R; \mu)$ is plotted for $\mu = 20, 15, 10$. Observe that whenever $\lambda_\mu(l, R; \mu) > 0$, $\lambda_\mu(l, R; \mu)$ is an increasing function of μ. This observation implies that a larger deposition flux is required to make the perturbations grow if desorption is increased. Correspondingly, a wider range of deposition fluxes results in the perturbation growth during shrinkage. This observation confirms our conclusions: desorption tends to stabilize the perturbations during growth, but on the other hand, helps to amplify the perturbations during shrinkage.

4.3. Effect of the far-field flux

We next analyze the effect of a constant far-field flux Ψ. It is expected that this far-field flux will affect the results when the island is close to the boundary ($R = 1$). We first remark that if we let

$$\Psi = \frac{(\mu^2 n_{\Gamma_\infty} - \Lambda)(\mu\xi_- C_1(0, R) + 2C_2(0, R))}{4\mu(C_3(0, 1) + \mu\xi_- C_4(1))},$$

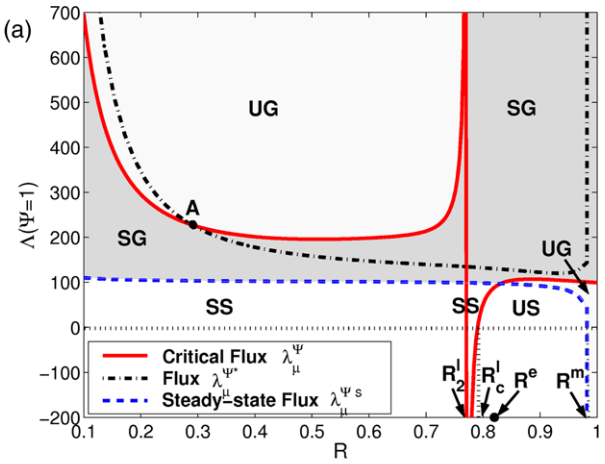

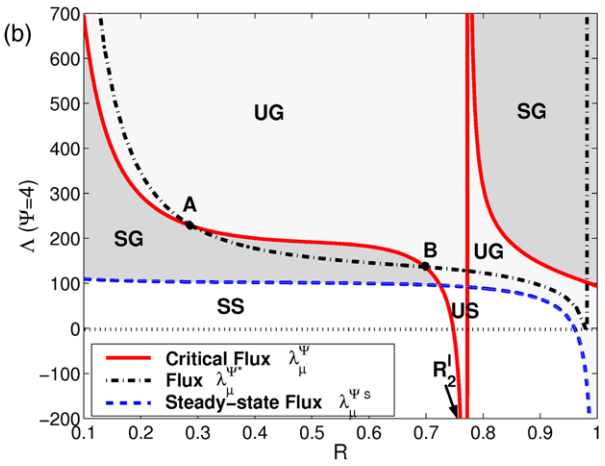

Fig. 9. Stability diagrams and fluxes $\lambda_\mu^{\Psi*}(l, R; \mu)$ in the (Λ, R)-plane with $\Psi = 1$ in (a) and $\Psi = 4$ in (b). In both (a) and (b), the curve $\Lambda = \lambda_\mu^{\Psi}(l, R; \mu)$ (solid), separates the stable growth region (shaded and marked by 'SG') and the unstable growth region (shaded and marked by 'UG'). It also separates the stable shrinkage region (marked by 'SS') and unstable shrinkage region (marked by 'US'), which is similar to the case wherein the far-field flux is absent. In contrast to the case with $\Psi = 0$, the curve no longer separates the stable growth region and unstable shrinkage region. The dash-dotted line plots the flux $\lambda_\mu^{\Psi*}(l, R; \mu)$ such that mode l is the fastest growing, if $\text{perrate}_\mu^{\Psi}(l, R; \mu, \lambda_\mu^{\Psi*}(l, R; \mu)) > 0$ (and the slowest decaying, if $\text{perrate}_\mu^{\Psi}(l, R; \mu, \lambda_\mu^{\Psi*}(l, R; \mu)) < 0$) among all modes. The dashed line plots the steady-state flux $\lambda_\mu^{\Psi s}(R; \mu)$, which separates the growth region and shrinkage region. The parameters are: $\mu = 10$, $\xi_- = 0.002$, $\rho^* = 1$, $\delta = 0.01$, $\beta = 10^{-4}$, $l = 5$.

where C_3 and C_4 are defined in Appendix B, then the adatom concentration at Γ_∞ is equal (at the level of the linear theory) to n_{Γ_∞}, where n_{Γ_∞} is the far-field boundary condition in [7] applied at a finite domain. The adatom concentration of the lower terrace ρ_-^{Ψ}, the velocity of the circle $\dot{R}^{\Psi}$, the growth rate of the perturbation perrate^{Ψ}, the critical flux λ^{Ψ}, and the flux $\lambda^{\Psi*}$ such that mode l is the fastest growing, if $\text{perrate}^{\Psi}(l, t, R; \lambda^{\Psi*}) > 0$ (and the slowest decaying, if $\text{perrate}^{\Psi}(l, t, R; \lambda^{\Psi*}) < 0$), and the corresponding quantities with desorption are all given in Appendix B.

In Fig. 9(a) and (b), two typical stability diagrams are plotted to demonstrate the effect of the far-field flux in the presence of desorption. In (a), $\Psi = 1$ while in (b), $\Psi = 4$, and the other

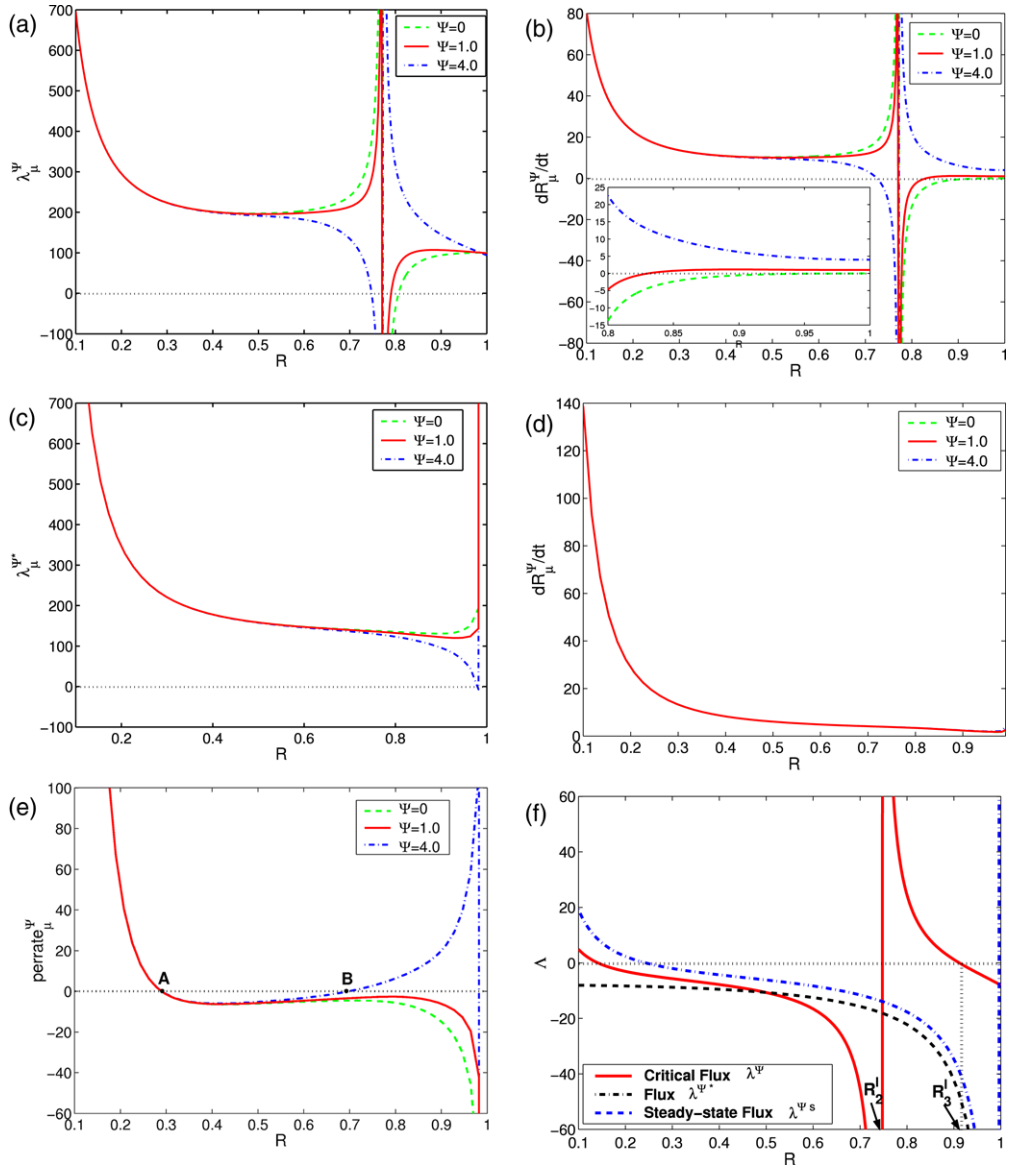

Fig. 10. Several results are plotted as functions of R for different far-field fluxes: $\Psi = 0, 1, 4$. (a) Critical fluxes $\lambda_\mu^\Psi(l, R; \mu)$. (b) The corresponding velocities of the underlying circle. (c) The fluxes $\lambda_\mu^{\Psi *}(l, R; \mu)$. (d) The corresponding velocities of the underlying circle. (e) Perturbation growth rates $\text{perrate}_\mu^\Psi(l, R; \mu, \lambda_\mu^{\Psi *}(l, R; \mu))$. (f) Stability diagram of the case without desorption and the flux $\lambda^{\Psi *}(l, R)$ in the (Λ, R)-plane with $\Psi = 4$. The parameters are: $\mu = 10$, $\xi_- = 0.002$, $\rho^* = 1$, $\delta = 0.01$, $\beta = 10^{-4}$, $l = 5$.

parameters are as in Fig. 5. We first remark that the regions ($R \in (0, 0.1)$), which are not shown for both cases, are almost identical to that of Fig. 5(a). Compared to the case without the far-field flux, an extra unstable growth region with $\Lambda > 0$ arises for $R > R_2^l$. We observe that this region appears very close to the boundary ($R = 1$), when Ψ is small (cf. (a)); and appears right after R_2^l, when Ψ is big (cf. (b)). This region arises because the steady-state flux $\lambda_\mu^{\Psi s}(R; \mu)$ (dashed line) diverges to $-\infty$ as $R \to 1$ due to $\Psi > 0$. Because of the presence of this unstable growth region, R_2^l is no longer a naturally stabilizing radius. Moreover, for $R < R_2^l$, the critical flux may also separate the stable shrinkage region and the unstable shrinkage region (cf. (b)), depending on the far-field flux. The dash-dotted lines represent the fluxes $\lambda_\mu^{\Psi *}(l, R; \mu)$. We observe that these fluxes blow up at boundary as in the case with $\Psi = 0$. Observe that when Ψ is large, and the flux $\Lambda = \lambda_\mu^{\Psi *}(l, R; \mu)$ is used, the evolution transits from unstable to stable growth at large R because of the blow up in $\lambda_\mu^{\Psi *}(l, R; \mu)$. We remark that, in the case without desorption, introducing the far-field flux may extend the unstable growth region up to some radius R_3^l (where $R_2^l < R_3^l < 1$), but the circular island will still stably grow for $R \in [R_3^l, 1)$ (cf. Fig. 10(f)).

In Fig. 10, several results are plotted to further demonstrate the dependence upon the far-field flux Ψ. Again, the regions ($R \in (0, 0.1)$) of all plots are omitted for the same reason as mentioned before. In (a), the critical fluxes from Fig. 5 ($\Psi = 0$), Fig. 9(a) and (b) are plotted together. We observe that the effect of far-field flux is minor when the circular island is small. The $\Psi = 1$ and $\Psi = 0$ critical fluxes are very similar for all R, while for $\Psi = 4$, the behavior is dramatically different for

large R. In Fig. 10(b), the corresponding velocities are plotted. In contrast to the case when Ψ is small, we observe that circular islands with large enough initial size (e.g. $R > R_2^l$) will grow up to the boundary when Ψ is large enough. In Fig. 10(c), the fluxes $\lambda_\mu^*(l, R; \mu)$ from Fig. 5 ($\Psi = 0$), $\lambda_\mu^{\Psi*}(l, R; \mu)$ from Fig. 9(a) and Fig. 9(b) are plotted, respectively. Again, deviations are observed when Ψ and R are large. In Fig. 10(d), the corresponding velocities are plotted. The velocities depend very weakly on Ψ. In Fig. 10(e), the corresponding perturbation growth rates are plotted. As seen in Fig. 9(b), observe that when Ψ is large, perturbations of large enough circular islands will grow nearly to the boundary ($R = 1$). This is contrast to the case with small Ψ. At the boundary $R = 1$, perrate$_\mu^\Psi$ diverges to $-\infty$, thus perturbations decay when the island's radius is very close to 1.

4.4. Application to shape control

During epitaxial growth, we may use the previous results and take advantage of the deposition flux Λ and possibly the far-field flux Ψ to control the shape of an island. To demonstrate the idea, we suggest the following two experiments.

4.4.1. Amplification of the perturbation during growth (with $\Psi = 4$)

In this experiment, we wish to amplify a specific mode $l = 5$ significantly during growth nearly up to the boundary ($R = 1$). To do this, we consider an initial island containing modes 3, 5 and 8 with initial radius $R(0) = r_0 = 0.1$, and initial perturbation $R_{1,l}(0) = 0.004$ for each mode. Note that this initial island radius r_0 is larger than the critical radius R_1^5 for mode 5 to grow. To begin, we first take the far-field flux $\Psi = 4$ as suggested by the analysis in the previous section. To make mode 5 grow the fastest, we should use the deposition flux $\Lambda = \lambda_\mu^{\Psi*}(5, R; \mu)$. However, as we have seen from Fig. 10(e), there exists a range of radii $r_1 \le R \le r_2$ (marked by 'A' and 'B'), where the perturbations decay, since $\lambda_\mu^{\Psi*}(5, R; \mu)$ is in the stable growth region (cf. Fig. 9(b)). Therefore, to prevent the decay of mode 5 in this region, it is natural to take the flux $\Lambda = \lambda_\mu^{\Psi}(5, R; \mu)$ in this interval, so that the 5th mode perturbation will remain unchanged for $r_1 \le R \le r_2$. For $R > r_2$, we may again take $\Lambda = \lambda_\mu^{\Psi*}(5, R; \mu)$ until the island is close to the boundary. Consequently, the 5th mode will achieve its greatest magnitude close to the boundary. The composite flux is plotted in Fig. 11(b). Note that one could further optimize the choice of fluxes to achieve the maximum possible growth of mode 5.

In Fig. 11(a), we present island morphologies that correspond to the choice of fluxes described above. The morphologies are shown at times $t_0 = 0$, $t_1 = 0.00666$, $t_2 = 0.0509399$, $t_3 = 0.1$, where the radii of the underlying circles are $r_0 = 0.1$, $r_1 = 0.2901$, $r_2 = 0.6981$, $r_3 = 0.8683$, respectively. Now that r_1 and r_2 are the radii that correspond to points A and B in Fig. 10(e). The emergence of a nearly five-fold symmetric island shape is seen and the perturbation becomes more pronounced as the island grows. In Fig. 11(c), the radii of the underlying circle during the evolution are plotted. In Fig. 11(d), the shape factors $R_{1,l}/R$ with $l = 3, 5$, and 8 are plotted. From this figure, it is clear that the 5th mode is dominant. Note however that between r_1 and r_2, mode 8 also grows after an initial period of decay while mode 3 decays. This is because of the existence of the two critical wavenumbers $l_c^*(R)$ and $l_c(R)$, as discussed in Section 4.2, such that perturbations with wavenumber $l \le l_c^*(R)$ or $l \ge l_c(R)$ decay or remain unchanged, while those with wavenumber $l_c^*(R) < l < l_c(R)$ grow. Taking $R \approx 0.6$, for example, yields $l_c^*(0.6) = 6$ and $l_c(0.6) = 11$, which indicates modes 7–10 are unstable, therefore confirming the result.

4.4.2. Amplification of the perturbation during shrinkage (with $\Psi = 1$)

In this experiment, we wish to take advantage of unstable shrinkage to amplify a specific mode $l = 5$. We therefore take $\Psi = 1$. See Fig. 9(a). Note that the unstable shrinkage domain corresponds to $R_c^l < R < R^m$, where R_c^l is the maximum zero of $\lambda_\mu^{\Psi}(l, R; \mu)$, and R^m is the zero of $\lambda_\mu^{\Psi s}(R; \mu)$. Again, see Fig. 9(a). We consider the same initial condition as in the previous experiment. To grow the island into the unstable shrinkage region, we use an analogous strategy as in the previous experiment. Again, this strategy could be further optimized to achieve the maximum growth. Initially, we take the flux $\Lambda = \lambda_\mu^{\Psi*}(5, R; \mu)$, so that mode 5 is the fastest growing mode. Then, at point A, where $\lambda_\mu^{\Psi*}(5, R; \mu) = \lambda_\mu^{\Psi}(5, R; \mu)$, we switch to the flux $\Lambda = \lambda_\mu^{\Psi}(5, R; \mu)$, so that mode 5 does not decay and instead remains unchanged. As the radius increases to R_2^5, when $\lambda_\mu^{\Psi}(5, R; \mu)$ diverges, we then switch back to the flux $\Lambda = \lambda_\mu^{\Psi*}(5, R; \mu)$. At this point, mode 5 will then start to decay as the island continues to grow. However, mode 5 will decay the slowest among all the modes. We then grow the island with this flux up to a radius $r_3 \approx 0.9$. At this point, we turn off the deposition flux by taking $\Lambda = 0$. This brings the evolution into the unstable shrinkage region. The island is then shrunk to a radius R^e which is slightly larger than R_c^5, and the perturbation grows. At $R = R^e$, we take again the flux $\Lambda = \lambda_\mu^{\Psi*}(5, R; \mu)$ and grow the island up to $R = r_3$ at which point we again take $\Lambda = 0$. We refer to this as a cycle. See Fig. 12(b) for a graph of the composite flux Λ. The idea is that the perturbation of the island increases over a flux cycle, therefore giving us control of the shape. We note that there is freedom in choosing the cycling points R^e and r_3.

In Fig. 12(a) the interface morphologies are shown that correspond to the flux described above. The times and radii shown are $t_0 = 0$, $t_1 = 0.006624$, $t_2 = 0.048$, $t_3 = 0.1$, $t_4 = 0.11$, $t_5 = 0.140905$, $t_6 = 0.1504077$, and $r_0 = 0.1$, $r_1 = 0.2896$, $r_2 = 0.7455$, $r_3 = 0.9045$, $r_4 = R^e = 0.8199$, $r_5 = r_3 = 0.9045$, $r_6 = R^e = 0.8199$, respectively. Two cycles are used to achieve the island plotted using the dashed curve. In one cycle, the perturbation of the 5th mode is amplified by about 9.347%. The amplification clearly seen in the figure and a five-fold dominant shape is observed. In Fig. 12(c), the radii of the underlying circle are plotted as a function of time. The radius decreases when the deposition flux $\Lambda = 0$. In Fig. 12(d), the shape factors $R_{1,l}/R$ with $l = 3, 5$, and 8 are plotted as functions of time. Observe that the 5th mode is

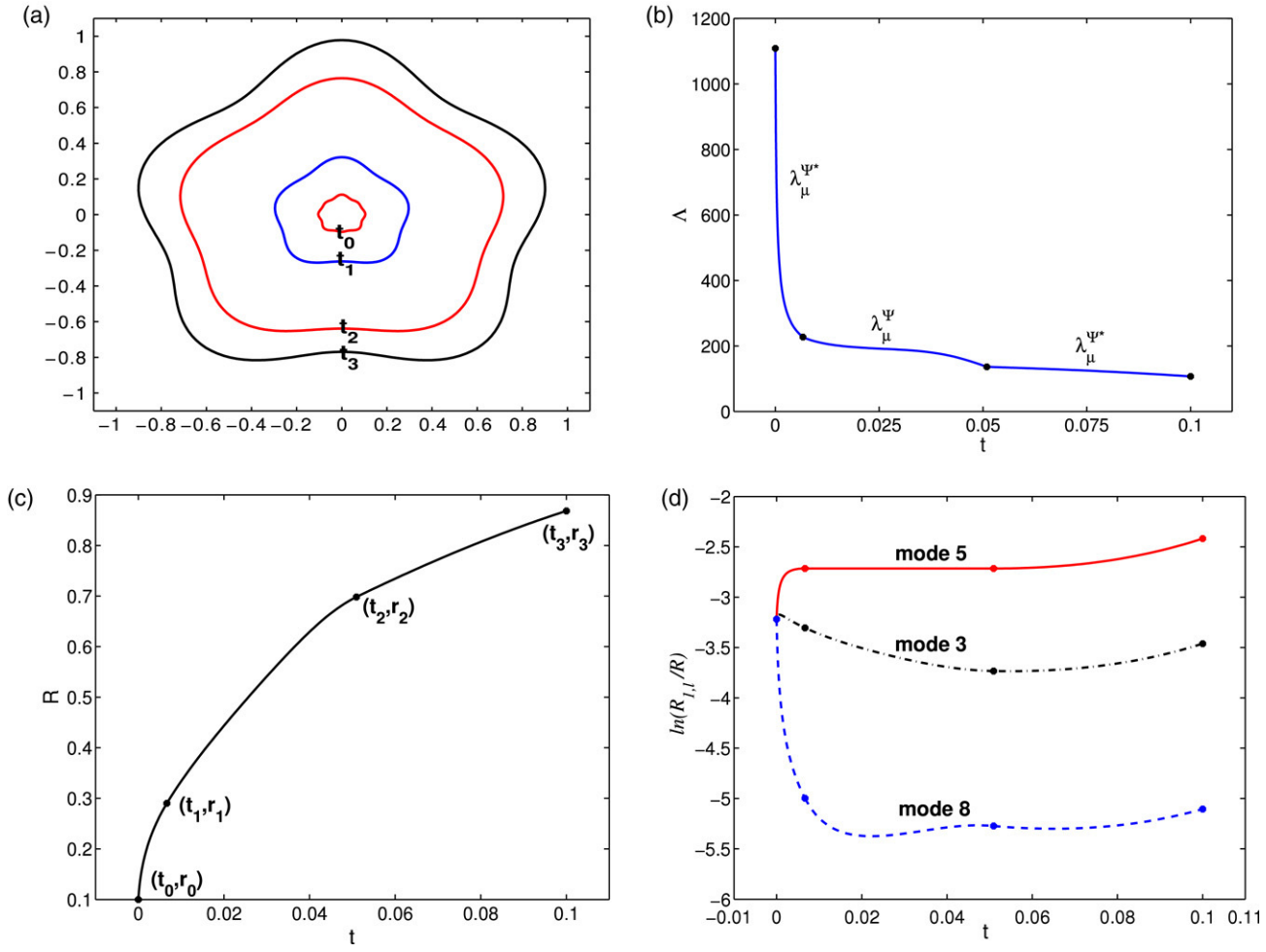

Fig. 11. Shape control during growth. Morphologies are based on solutions from the linear theory. (a) The evolution of morphologies of an island containing modes: $l = 3, 5$ and 8 under the flux shown in (b). The times shown are $t_0 = 0$, $t_1 = 0.00666$, $t_2 = 0.0509399$, $t_3 = 0.1$. The initial radius is $R(0) = 0.1$ and the initial perturbation is $R_{1,l}(0) = 0.004$. The parameters are: $\Psi = 4$, $\mu = 10$, $\xi_- = 0.002$, $\rho^* = 1$, $\delta = 0.01$, $\beta = 10^{-4}$, $l = 3, 5, 8$. (b) The flux. (c) The radii of the underlying circle during the evolution versus time. (d) The evolution of the shape factors $R_{1,l}/R$ versus time.

dominant and that both the 5th and 3rd modes are amplified during the unstable shrinkage.

4.5. Brief discussion on the two-sided model with desorption and far-field flux

Adatom diffusion inside the island and the corresponding attachment kinetics at the island boundary can easily be incorporated into the stability analysis presented previously for the one-sided model. However, the analytical formulas for important quantities such as the critical flux $\lambda_\mu^\Psi(l, R; \mu)$ and the flux $\lambda_\mu^{\Psi*}(l, R; \mu)$, become unwieldy due to their complicated form. Nevertheless, as we demonstrate below, the two-sided system qualitatively behaves very much like the one-sided problem ($\xi_+ = \infty$) in the following sense. First, both critical radii R_1^l and R_2^l exist. Secondly, unstable shrinkage and unstable growth exist beyond R_2^l. However, quantitatively, both R_1^l and R_2^l may shift to different values due to the kinetic attachment rate ξ_+ which generates fluxes from the upper terrace to stabilize the growth. Also, since the far-field flux is the primary cause of unstable growth close to the boundary, a larger far-field flux than the one used in the one-sided case is required to achieve unstable growth when ξ_+ is finite.

In Fig. 13, two typical stability diagrams for the two-sided model with the desorption and far-field flux are plotted with parameters: $\mu = 10$, $\xi_- = 0.002$, $\rho^* = 1$, $\delta = 0.01$, $\beta = 10^{-4}$, $l = 5$. In (a) and (b), $\xi_+ = 0.002$ and $\Psi = 1$, in (c) and (d), $\xi_+ = 0.002$ and $\Psi = 400$. We first observe that the results are qualitatively similar to Fig. 5(b), in which $\xi_+ = +\infty$ and $\Psi = 0$. It is clear that R_2^l still appears but dramatically shifts to a smaller value when $\xi_-/\xi_+ = 1$ compared to the case in which $\xi_-/\xi_+ = 0$ (shown in Fig. 5(b)). Actually, a detailed analysis shows that R_1^l and R_2^l are increasing and decreasing functions of ξ_-/ξ_+, respectively. This means that the one-sided case actually gives the widest unstable growth region of radii. Secondly, in contrast to Fig. 9(a), letting the far-field flux equal to 1 does not create an extra unstable growth region for large radii. This is because, the kinetic attachment rate from the upper terrace ξ_+ is an additional stabilizing factor, and therefore, a larger far-field flux is required to increase the perturbations. This point is supported by the next set of plots Fig. 13(c) and (d). Clearly, (c), together with (d) are similar to Fig. 9(a). We remark, one

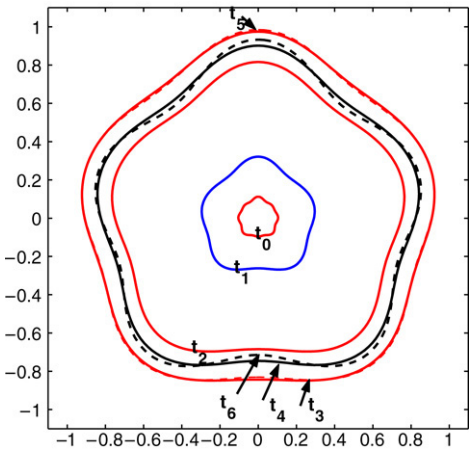

(a) The evolution of morphologies of an island containing modes: $l = 3$, 5 and 8 under the flux shown in Fig. 12(b). The times shown are $t_0 = 0$, $t_1 = 0.006624$, $t_2 = 0.048$, $t_3 = 0.1$, $t_4 = 0.11$, $t_5 = 0.140905$, $t_6 = 0.1504077$, with corresponding radii: $r_0 = 0.1$, $r_1 = 0.2896$, $r_2 = 0.7455$, $r_3 = 0.9045$, $r_4 = R^e = 0.8199$, $r_5 = r_3 = 0.9045$, $r_6 = R^e = 0.8199$, respectively. Where the initial radius is $R(0) = r_0 = 0.1$, and the initial perturbation is $R_{1,l}(0) = 0.004$. The parameters are: $\Psi = 1$, $\mu = 10$, $\xi_- = 0.002$, $\rho^* = 1$, $\delta = 0.01$, $\beta = 10^{-4}$, $l = 3, 5, 8$.

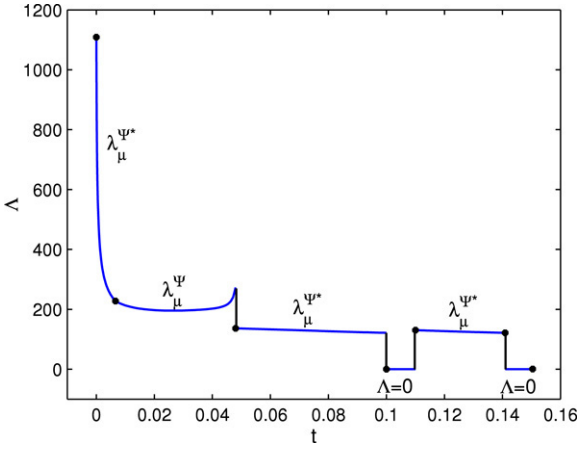

(b) The flux.

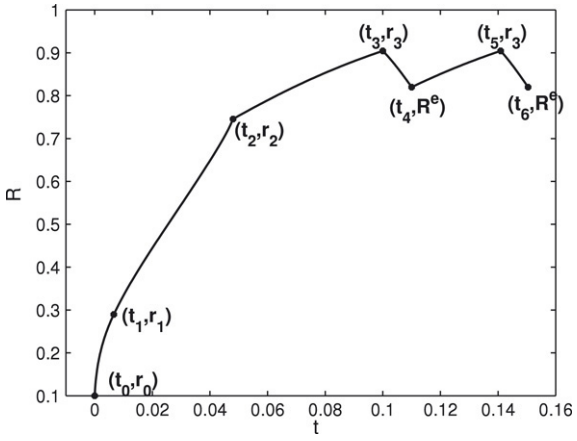

(c) The radii of the underlying circle during the evolution versus time.

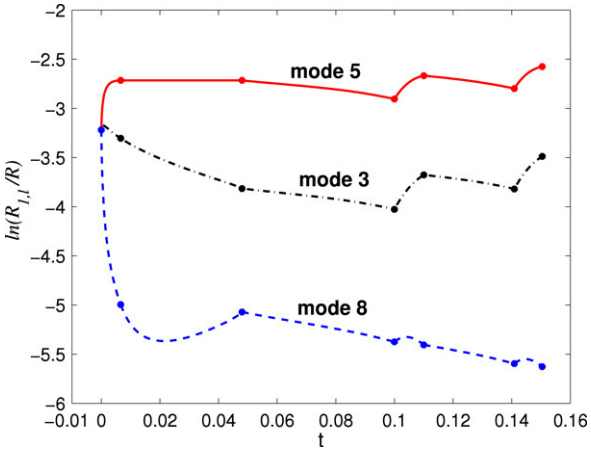

(d) The evolution of the shape factors $R_{1,l}/R$ versus time.

Fig. 12. Shape control during shrinkage. Morphologies are based on solutions from the linear theory.

should expect an even larger far-field flux is needed to create a similar growth as shown in Fig. 9(b).

One may also perform shape control applications for the two-sided model in an analogous manner as that presented for the one-sided model in Section 4.4. As suggested by the results above, the far-field flux Ψ must be chosen sufficiently large to do this though. We also note that for certain parameter ranges in the two-side case, the flux $\lambda_\mu^{\Psi*}(l, R; \mu)$ may actually correspond to the fastest decaying mode when $\text{perrate}_\mu^\Psi(l, t, R; \mu, \lambda_\mu^{\Psi*}(l, R; \mu)) < 0$ in contrast to the one-sided case where $\lambda_\mu^{\Psi*}(l, R; \mu)$ corresponds to the slowest decaying mode when $\text{perrate}_\mu^\Psi(l, t, R; \mu, \lambda_\mu^{\Psi*}(l, R; \mu)) < 0$. However, for the parameters taken in Fig. 13(a) and (c), we have checked that the behavior is similar to the one-sided case and the strategy outlined in Section 4.4 can be used to control the island morphologies by amplifying a specific mode.

5. Conclusions and future work

In this paper, we performed a complete analysis of the morphological stability of a single, epitaxially growing perturbed circular island using a BCF model. By focusing on a one-sided model, where the adatom concentration is constant in the island, we determined the critical flux for which the shape of the island, when perturbed by a single mode, remains unchanged during the evolution. This critical flux depends on the island radius and the mode wavenumber (as well as

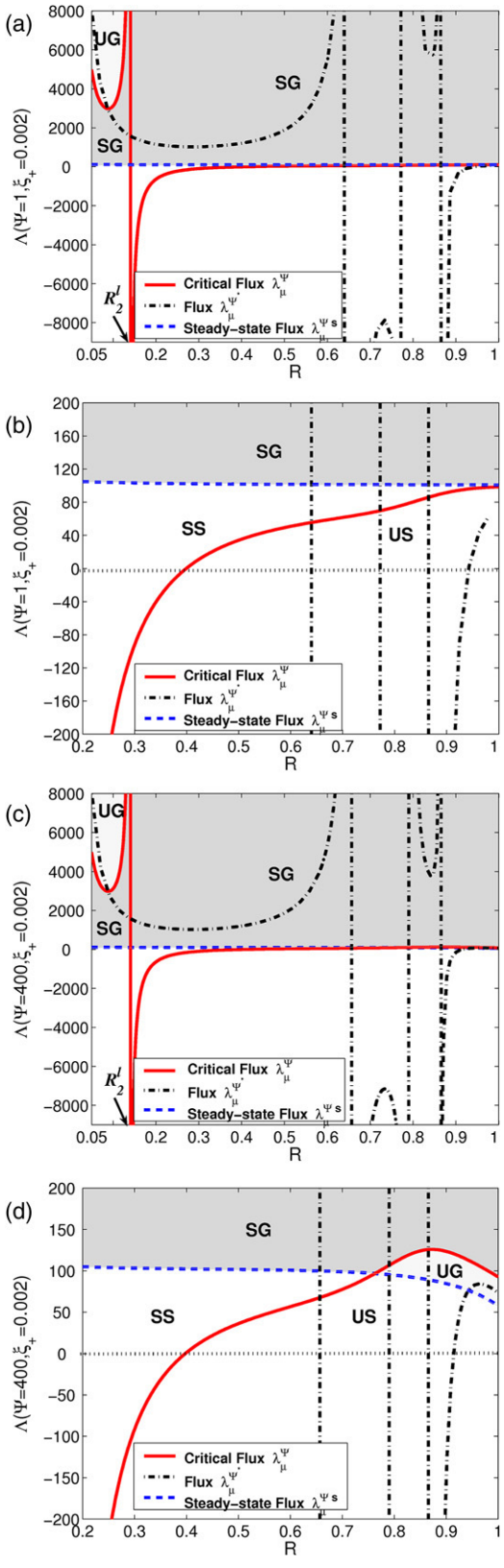

Fig. 13. Stability diagrams and fluxes $\lambda_\mu^{\Psi *}(l, R; \mu)$ in the (Λ, R)-plane for the two-sided model with $\Psi = 1, \xi_+ = 0.002$ in (a), (b); $\Psi = 400, \xi_+ = 0.002$ in (c), (d), where (b) and (d) are two close-ups. The parameters are: $\mu = 10$, $\xi_- = 0.002$, $\rho^* = 1$, $\delta = 0.01$, $\beta = 10^{-4}$, $l = 5$.

other parameters). We also determined the flux that makes a specific mode the fastest growing (or slowest decaying when the perturbation is decreasing) among all the modes. In the absence of an additional far-field mass flux, small islands are always stable if kinetics is present, even without the line tension or surface diffusion, and there exists a naturally stabilizing radius beyond which the growth is always stable. Up to this naturally stabilizing radius, taking fluxes larger than the critical flux result in instability. In the presence of desorption, a new regime is introduced in which the island may shrink stably, or unstably, with non-negative deposition fluxes. The presence of an additional uniform far-field flux, may eliminate the naturally stabilizing radius and results in unstable growth at all radii. We also demonstrated that the behavior of the full two-sided model is qualitatively similar to that of the one-sided case which is easier to analyze, and represents the most unstable growth case. We then presented examples of how these results may be used to control the shape of the island using the deposition and far-field fluxes as control parameters.

In future work, we plan to characterize the non-linear evolution of islands to determine the extent of applicability of our linear stability theory and ideas on shape control at the nanoscale. To perform non-linear studies, we will develop diffuse -interface methods based on our previous work in [17], where we devised such models for perturbations of straight steps. In these diffuse-interface models, we will also explore the nucleation of new island either on top of or near the initial island and determine the effect on growth. Finally, in future work, we plan to investigate the effect of elastic interactions of the island dynamics.

Acknowledgments

The authors thank Axel Voigt for valuable discussions and for bringing this problem to our attention. The authors gratefully acknowledge partial support from the University of Minnesota Sponsored Projects Office and the National Science Foundation Division of Mathematical Sciences and the Division of Materials Research. Z. Hu was also partially supported by a Doctoral Dissertation Fellowship from the Graduate School at the University of California, Irvine. The authors also acknowledge the generous computing resources from the Network and Academic Computing Services.

Appendix A

Let us consider $R > R_2^l$, according to Observation 2, we know $g_\mu(l, R; \mu) < 0$. Now let $f_\mu(l, R; \mu) = \frac{\mu\rho^*\delta(l^2-1)}{4R}(\mu\xi_- C_1(0, R) + 2C_2(0, R))C_1(l, R)$, then by Eq. (43), $q_\mu(l, R; \mu) = \frac{\beta l^2(l^2-1)}{R^4}h_\mu(l, R; \mu) + \mu^2\rho^*(1 + \frac{\delta}{R})g_\mu(l, R; \mu) + f_\mu(l, R; \mu)$. Since $g_\mu(l, R; \mu) < 0$ for $R > R_2^l$, we then get $q_\mu(l, R; \mu) < 0$ if and only if

$$\mu^2 > \frac{-\frac{\beta l^2(l^2-1)}{R^4}h_\mu(l, R; \mu) - f_\mu(l, R; \mu)}{\rho^*\left(1 + \frac{\delta}{R}\right)g_\mu(l, R; \mu)}. \tag{44}$$

It is hard to find the explicit solution to Eq. (44), but numerically, we notice that $-f_\mu(l, R; \mu)/g_\mu(l, R; \mu)$ and $-h_\mu(l, R; \mu)/g_\mu(l, R; \mu)$ decrease to 0 and 1 rapidly as R goes to 1, respectively. Therefore, when the non-dimensional

radius R is large, one can simply take a μ, such that $\mu^2 > \frac{\beta l^2(l^2-1)}{\rho^*(1+\delta)}$ to guarantee that, there exists a radius $R_c^l \in (R_2^l, 1)$ such that $q_\mu(l, R; \mu) < 0$ for $R \in (R_c^l, 1)$, and consequently $\lambda_\mu(l, R; \mu) > 0$ for $R \in (R_c^l, 1)$.

Appendix B

We now present the solutions to Eqs. (18)–(25) in presence of the far-field flux.

Without desorption. The adatom concentration of the lower terrace ρ_-^Ψ, the velocity of the circle $\dot{R}^\Psi$, the growth rate of the perturbation perrate$^\Psi$, the critical flux λ^Ψ, and the flux $\lambda^{\Psi*}$ such that mode l is the fastest growing, if perrate$^\Psi(l, t, R; \lambda^{\Psi*}) > 0$ (and the slowest decaying, if perrate$^\Psi(l, t, R; \lambda^{\Psi*}) < 0$) are given as follows:

$$\rho_-^\Psi(r, t) = \rho_-(r, t) + \Psi \ln\left(\frac{r}{R}\right) + \frac{\xi_- \Psi}{R},$$

$$\dot{R}^\Psi(t) = \dot{R}(t) + \frac{\Psi}{R},$$

$$\lambda^{\Psi s}(R) = -\frac{2\Psi}{1-R^2},$$

$$\text{perrate}^\Psi(l, t, R; \Lambda) = \frac{g(l, R)}{h(l, R)}(\Lambda - \lambda^\Psi(l, R)),$$

$$\lambda^\Psi(l, R) = \lambda(l, R) + \frac{2\Psi(2R(1+R^{2l}) - l(R-\xi_-)(1-R^{2l}))}{g(l, R)},$$

$$\lambda^{\Psi*}(l, R) = \lambda^*(l, R) - \frac{2\Psi(R+\xi_-)}{R(1-R^2)+\xi_-(1+R^2)},$$

where $\rho_-(r, t)$, $\dot{R}(t)$, $g(l, R)$, $h(l, R)$, $\lambda(l, R)$, and $\lambda^*(l, R)$ are defined in Section 3.1.

With desorption. The corresponding quantities with desorption are given below:

$$\omega_-^\Psi(r, t; \mu) = \omega_-(r, t; \mu) + \frac{4\mu\Psi(C_3(0, r) + \mu\xi_- C_4(r))}{\mu\xi_- C_1(0, R) + 2C_2(0, R)},$$

$$\dot{R}_\mu^\Psi(t; \mu) = \dot{R}_\mu(t; \mu) + \frac{4\Psi C_4(R)}{\mu\xi_- C_1(0, R) + 2C_2(0, R)},$$

$$\lambda_\mu^{\Psi s}(R; \mu) = \lambda_\mu^s(R; \mu) - \frac{4\mu\Psi C_4(R)}{C_1(0, R)},$$

$$\text{perrate}_\mu^\Psi(l, t, R; \mu, \Lambda) = \frac{g_\mu(l, R; \mu)}{h_\mu(l, R; \mu)}(\Lambda - \lambda_\mu^\Psi(l, R; \mu)),$$

$$\lambda_\mu^\Psi(l, R; \mu) = \lambda_\mu(l, R; \mu) - \frac{\Psi(R-\xi_-)C_1(l, R)}{Rg_\mu(l, R; \mu)} - \frac{\Psi(\mu^2R^2C_3(2, R) + 2\mu^2R\xi_- - 2)C_2(l, R)}{\mu R g_\mu(l, R; \mu)},$$

$$\lambda_\mu^{\Psi*}(l, R; \mu) = \lambda_\mu^*(l, R; \mu) + \frac{\mu\Psi(2\mu\xi_-^2 + 2\mu\xi_- RC_3(2, R) + 2R(\mu^2\xi_-^2 - 2)C_4(R))}{(R+\xi_-)C_1(0, R) + 2\mu\xi_- RC_2(0, R)},$$

where

$$C_3(l, r) = K(0, \mu R)I(l, \mu r) - I(0, \mu R)K(l, \mu r),$$

$$C_4(r) = I(1, \mu R)K(0, \mu r) + K(1, \mu R)I(0, \mu r),$$

and $\omega_-(r, t; \mu)$, $\dot{R}_\mu(t; \mu)$, $g_\mu(l, R; \mu)$, $h_\mu(l, R; \mu)$, $\lambda_\mu(l, R; \mu)$, and $\lambda_\mu^*(l, R; \mu)$ are defined in Section 3.2.

References

[1] W. Burton, N. Cabrera, F. Frank, The growth of crystals and the equilibrium structure of their surfaces, Philos. Trans. R. Soc. Lond. Ser. A 243 (1951) 299–358.

[2] X.L. Wang, V. Voliotis, Epitaxial growth and optical properties of semiconductor quantum wires, J. Appl. Phys. 99 (2006) 121301.

[3] H.E. Katz, Recent advances in semiconductor performance and printing processes for organic transistor-based electronics, Chem. Mater. 16 (2004) 4748–4756.

[4] G.S. Bales, A. Zangwill, Morphological instability of a terrace edge during step-flow growth, Phys. Rev. B 41 (1990) 5500–5508.

[5] R.E. Caflisch, W. E, M.F. Gyure, B. Merriman, C. Ratsch, Kinetic model for a step edge in epitaxial growth, Phys. Rev. E 59 (1999) 6879.

[6] R.E. Caflisch, B. Li, Analysis of island dynamics in epitaxial growth of thin films, Multiscale Model. Simul. 1 (2003) 150–171.

[7] M. Avignon, B.K. Chakraverty, Morphological stability of two-dimensional nucleus, Roy. Soc. London 310 (1969) 277–296.

[8] W.W. Mullins, R.F. Sekerka, Morphological stability of a particle growing by diffusion or heat flow, J. Appl. Phys. 34 (1963) 323.

[9] G.S. Bales, D.C. Chrzan, Transition from compact to fractal islands during submonolayer epitaxial growth, Phys. Rev. Lett. 74 (1995) 4879–4882.

[10] V. Cristini, J. Lowengrub, Three-dimensional crystal growth-I: Linear analysis and self-similar evolution, J. Crystal Growth 240 (2002) 267.

[11] S. Li, J. Lowengrub, P. Leo, V. Cristini, Nonlinear theory of self-similar crystal growth and melting, J. Crystal Growth 267 (2004) 703.

[12] B. Li, A. Rätz, A. Voigt, Stability of a circular epitaxial island, Physica D 198 (2004) 231–247.

[13] J. Krug, Introduction to step dynamics and step instabilities, in: A. Voigt (Ed.), Multiscale Modeling in Epitaxial Growth, Birkhauser, 2005, pp. 69–96.

[14] R. Ghez, S.S. Iyer, The kinetics of fast steps on crystal surfaces and its application to the molecular beam epitaxy of silicon, IBM J. Res. Develop. 32 (1998) 804.

[15] K. Morgenstern, G. Rosenfeld, G. Comsa, Decay of two-dimensional Ag islands on Ag(111), Phys. Rev. Lett. 76 (1996) 2113–2116.

[16] W. Theis, N.C. Bartelt, R.M. Tromp, Chemical potential maps and spatial correlations in 2D-island ripening on Si(001), Phys. Rev. Lett. 75 (1995) 3328–3331.

[17] J. Lowengrub, Z. Hu, S. Wise, J. Kim, A. Voigt, Phase-field modeling of step dynamics, in: Proc. MRS. Soc., vol. 859E, Materials Research Society, Boston, MA, 2004, JJ8.6.1–6.